9-16-2021

DESIGN OF A CUSTOM DIGITAL LIGHT PROJECTION PRINTER FOR IN-SITU PRODUCTION OF COMPOSITES WITH IMPROVED THERMOMECHANICAL PROPERTIES

Margaret Anne Gillan
Rowan University

DESIGN OF A CUSTOM DIGITAL LIGHT PROJECTION PRINTER FOR IN-SITU PRODUCTION OF COMPOSITES WITH IMPROVED THERMOMECHANICAL PROPERTIES

by
Margaret Anne Gillan

A Thesis

Submitted to the
Department of Chemical Engineering
College of Engineering
In partial fulfillment of the requirement
For the degree of
Master of Science in Chemical Engineering
at
Rowan University
August 19, 2021

Thesis Chair: Joseph F. Stanzione III, Ph.D.

Committee Members:
Nicholas J. Alvarez, Ph.D.
Francis (Mac) Haas, Ph.D.
James A. Newell, Ph.D.

Acknowledgments

First, I would like to acknowledge and sincerely thank my advisor, Prof. Joseph F. Stanzione, III, for his guidance, support, and mentorship throughout my journey here at Rowan. Thank you for believing in me.

I would also like to thank my colleagues in the laboratory. Without your support, whether technical or personal, this work would not have been possible. I would especially like to acknowledge Dr. Alexander Bassett, Alexandra Chong, and Tristan Bacha, who provided extensive support and brainstorming sessions. Thank you for always being willing to listen and brainstorm with me, even when you thought I was way out in left field. A big thank you also goes out to my cohort and fellow AMMI team, including Dr. Elyse Baroncini, John Chea, Amit Dhundi, Kelli Hambleton, Rachael Ross, Matthew Schwenger, Kayla Sweet, and Jasmin Vasquez. I could not have asked for a more encouraging, supportive group in which to do this work.

I would also like to express my sincere gratitude to my committee, including Prof. Nicolas Alvarez, Prof. Mac Haas, and Prof. James Newell. Thank you for your support and guidance during my time here at Rowan. I would also like to thank the U.S. Army Combat Capabilities Development Command- Army Research Laboratory for their generous financial support via cooperative agreement W911NF-17-2-0227.

Finally, this work would not have been possible without the unrelenting love and support from my husband, Baruch Turniansky. Thank you for always encouraging me and pushing me to believe in myself.

Abstract

Margaret Anne Gillan
DESIGN OF A CUSTOM DIGITAL LIGHT PROJECTION PRINTER FOR IN-SITU PRODUCTION OF COMPOSITES WITH IMPROVED THERMOMECHANICAL PROPERTIES
2020-2021
Joseph F. Stanzione, III
Master of Science in Chemical Engineering

This work seeks to improve upon the existing state-of-the-art for vat photopolymerization additive manufacturing; namely, producing in-situ composites that combine the precision and high-performance materials of the vat photopolymerization with the strength of fiber-reinforced polymer composites. A custom-designed digital light projection printer was designed and built for printing composites, which includes an automated fiber tape system to place woven E-glass fiber mats in-situ. To validate the performance improvement of composites versus the neat matrix, composites were fabricated on the custom printer with hand-placed fiber mats. A high-performance, dual-cure resin was used for these studies. The effect of layer height on matrix properties was evaluated, and there was no statistically significant difference in glass transition temperature (T_g) or glassy storage modulus (E') at 25 °C as a function of layer height. It was found that composites exhibited up to a 25% improvement in E' relative to the matrix (2.9 versus 3.7 GPa) at a fiber volume fraction of 4-6% and a layer height of 200 μm. All composites exhibited a slightly lower T_g relative to the matrix (105 vs. 115 °C), but there is a minimal loss of thermal properties in the composites and a modest improvement in storage modulus, even with low fiber fraction. These results suggest that parts produced with the custom printer have the potential for high-strength military applications.

Table of Contents

Table of Contents (Continued)

Table of Contents (Continued)

List of Figures

List of Tables

Chapter 1

Introduction and Overview

1.1 Overview and Organization

Composite materials have been used for millennia, first dating to 3400 B.C. when ancient Mesopotamians used wood strips glued together at different angles to make plywood [1, 2]. In the following centuries, civilizations throughout the world used mud/straw and wood/clay composites as building materials. In 1200 A.D., Mongolian warriors made composite bows out of bamboo, silk, cattle tendons and horns, and pine resin [1, 2]. Polymer-matrix composites did not become possible until the early 20th century, with the conception of polymers such as vinyl, polystyrene, polyesters, and phenolic resins [2]. These polymers far outperformed the incumbent nature-derived materials. However, their lack of strength for structural applications limited their implementation. The development of fiberglass by Corning in 1935 marked a turning point for the world of polymers and the first glass-fiber reinforced composites were produced soon after [1, 2]. WWII also provided an important early market for composites as militaries sought out lightweight, strong materials. By the 1970s, fueled by the advent of Kevlar by Dupont in 1964 and high-quality carbon fiber in 1963 by the UK Ministry of Defence, the composites industry claimed a lasting foothold in the global materials market [2].

Composite materials are a critically important part of the global materials market. The U.S. composite end products market was valued at $26.7 billion in 2019 and is expected to grow to $33.4 billion by 2025 [3]. Fiber-reinforced polymer composites

(FRPCs) are used in broad structural and manufacturing applications, including aircraft and military, space, automotive, sporting goods, marine, construction, transportation, and infrastructure, among others [4-6]. Glass fiber is a common component of these FRPCs, and in 2017 the glass fiber market reached 2.5 billion pounds globally [5]. Glass fibers are the most common type of fiber reinforcing material for FRPCs [4]. Glass fibers are inexpensive, strong, have high chemical resistance, and are electrically insulating. Their main disadvantages are that they have a low modulus and high density relative to other fiber feedstocks, are sensitive to abrasion during handling, and their high hardness causes wear on equipment. However, many of these issues can be mitigated through judicious selection of the polymer matrix.

Fiber-reinforced polymer composites, including those containing glass fiber mats, continue to be relevant for military and industrial applications. This thesis work seeks to marry the strength and lightweighting effects of fiber-reinforced composites with the precision of vat photopolymerization additive manufacturing. Military interest in composites has only grown since the initial use of composites in WWII. Composites provide lightweight material options for equipment, non-structural components, structural components, and armor. Additive manufacturing in conjunction with composite materials can offer increased precision and part complexity compared to traditional manufacturing methods. This adds additional capability for lightweighting through part geometry, e.g. including hollow or meshed areas [7-9]. These benefits extend beyond the military and can be applied to other fields that make use of composites, including space, automotive, sporting goods, marine, construction, transportation, and infrastructure.

Continuous fiber reinforcements add strength along the axis of the fiber which is advantageous compared to randomly aligned fibers. Printing with continuous fibers is currently feasible in fused filament fabrication (FFF) printers such as the Markforged line of printers [10, 11]. However, the thermoplastics utilized in FFF-style printers often do not reach the thermal and mechanical performance metrics for military, aerospace, automotive, and other demanding applications. For this work, vat photopolymerization (VPP) additive manufacturing was chosen as the focus due to its high-strength and -stiffness materials. Fiber-reinforced composite resins for VPP are well-represented in both industrial formulations and the literature [12-24]. However, these resins typically contain only short, chopped fibers, and do not achieve the strength enhancement that continuous fiber feedstocks provide. We seek to address this gap through both instrumentation and process design. A custom VPP printer was designed and built to incorporate continuous fiber woven fiberglass mats into VPP prints. The design and operation of this printer are described. Additionally, the feasibility of incorporating these woven mats into an existing dual-cure sequential IPN resin system is demonstrated. The effect of layer height on the matrix-only DMA properties is reported, and effects of fiber fraction on composites fabricated are also reported. Chapter 1 introduces the appropriate background for traditional composite manufacturing techniques, general additive manufacturing, and VPP technologies.

1.2 Traditional Composite Fabrication Techniques

Fiber-reinforced polymer composites are produced via several industrially relevant methods ranging from very simple, as in open molding, to more complicated, as

in pultrusion or resin transfer molding [2, 4, 6]. Generally, any FRPC process involves fiber placement, addition of the resin matrix, consolidation, and finally a curing step. Fibers can be placed either by hand (hand layup) or in an automated process, of which there are many variations. Fiber feedstocks may also be dry or pre-pregs which are filled with a beta-cured resin. Once the fibers and matrix are combined, the part is consolidated, either by hand-rolling or application of pressure, e.g. in an autoclave. This consolidation step ensures that there is a minimum of voids present in the part and that the fibers are fully wet out with the resin. Consolidation also prevents defects like resin-rich areas, resin-poor areas, and inter-ply cracks [4, 6]. Finally, the resin is cured. Curing can occur very simply at room temperature and pressure, or heat and/or pressure can be applied to further the conversion of the resin, lower liquid resin viscosity, speed up curing, and minimize the presence of voids. The following sections describe common composite molding techniques using liquid resins, in order of volume/production speed.

Open molding is a commonly used technique for large, low-precision, and simple shapes like boat hulls, boat decks, bathtubs, shower stalls, etc. [2, 4, 6]. As the name suggests, an open-face mold is filled with the composite material, either by hand-layup or by semi-automated sprayup. Hand-layup involves hand-placing mats of fiber material, either dry or pre-pregs filled with beta-cured resin, into the mold before applying the resin matrix. A semi-automated sprayup technique is possible whereby a mixture of resin and chopped fibers are sprayed into the mold using a chopper gun. Typically, the composite is then consolidated by hand, and curing proceeds either in an oven or under ambient conditions.

Transfer molding techniques including resin transfer molding (RTM) and vacuum-assisted resin transfer molding (VARTM) are also commonly used composite fabrication techniques [2, 4, 6]. In these processes, a pre-formulated liquid resin is added to a mold containing dry fibers in a closed mold. The liquid resin must have a low enough viscosity to wet out the fibers and minimize the formation of voids and other defects. As the resin flows, it displaces air and fills in the spaces between fibers. Once the fibers are fully wet out, the resin is cured, and a composite part is produced. VARTM differs from RTM in that it makes use of a vacuum to evacuate air from the mold. This technique is commonly used with high-viscosity resins that may not flow well enough without assistance. As with other techniques, the resin is cured using heat and/or pressure, and the resulting part is removed from the mold.

Compression molding is an additional common FRPC fabrication technique that makes use of liquid thermosetting resins. Compression molding provides the ability to make complex geometries, including nonuniform thickness, ribs, bosses, flanges, holes, and shoulders [4, 6]. It is also a comparatively high-volume technique, allowing for many parts to be made faster than the previously described methods. The molds for compression molding typically consist of two parts: the lower, fixed mold, and an upper moveable mold half. Molds are heated to reduce the viscosity of the resin, enabling better wet-out of the fiber reinforcements, and to catalyze the curing reaction. To form the part, a sheet-molding compound is cut and stacked inside the pre-heated mold. The mold is closed and pressurized. The resin inside the sheet-molding compound is then able to flow

and expel air. Once the part is cured enough to hold its shape, it is removed from the mold.

Pultrusion is also a high-volume technique but proceeds quite differently than molding techniques [2, 4, 6, 25]. Pultrusion results in a long, straight profile that can be sliced into individual parts. It is commonly used for structural components. In a pultrusion process, fibrous material is pulled through a resin bath, then formed into the desired shape by passing through a series of forming guides and bushings. The material is then pulled through a heated die, which cures the resin. The pultruded profile is sliced into profiles of the appropriate length. Generally, there is minimal postprocessing required and there is no need for sanding, trimming, or postcuring. While other methods make use of pressurized curing conditions, pultrusion occurs at ambient pressure. However, previous work has demonstrated that the pressure in the die entrance zone is 250-1250 psi [25], likely high enough to minimize the presence of voids. This pressure is due to competing volumetric expansion of the heated resin and polymerization shrinkage. These forces can be balanced with judicious selection of resin chemistry and fiber volume fraction.

1.3 Additive Manufacturing

Additive manufacturing (AM) is a rising manufacturing technique due to its high precision, speed, and ability to utilize different materials. Common AM techniques include fused deposition modeling, direct ink writing, selective laser melting, and vat photopolymerization (VPP) or stereolithography (SLA). Figure 1 shows a schematic of each of these techniques. Traditionally, AM has been used for rapid prototyping, where a

prototype part is designed and printed on a 3D printer. The part is evaluated for fit and function, then the final part is produced using a more traditional manufacturing method like injection molding, casting, etc. [26, 27]. However, with advances in materials development and instrumentation, 3D printed parts are of high quality and can often serve as the final part, with no need for final production using another technology [28-32]. All additive manufacturing techniques involve building material in a layer-by-layer fashion to form a 3D part. This contrasts with subtractive or formative manufacturing. In subtractive manufacturing, a part is produced by taking away material from a large enough block to make the part until the desired shape remains. Formative manufacturing involves filling a mold with material, then breaking away the mold to produce a finished part. Examples of formative manufacturing include resin transfer molding techniques, injection molding, and blow molding. AM is generally more material-efficient compared to subtractive methods since there is little or no material waste. Additionally, AM can be more energy-efficient than traditional manufacturing techniques [33-36].

Figure 1

Additive Manufacturing Techniques

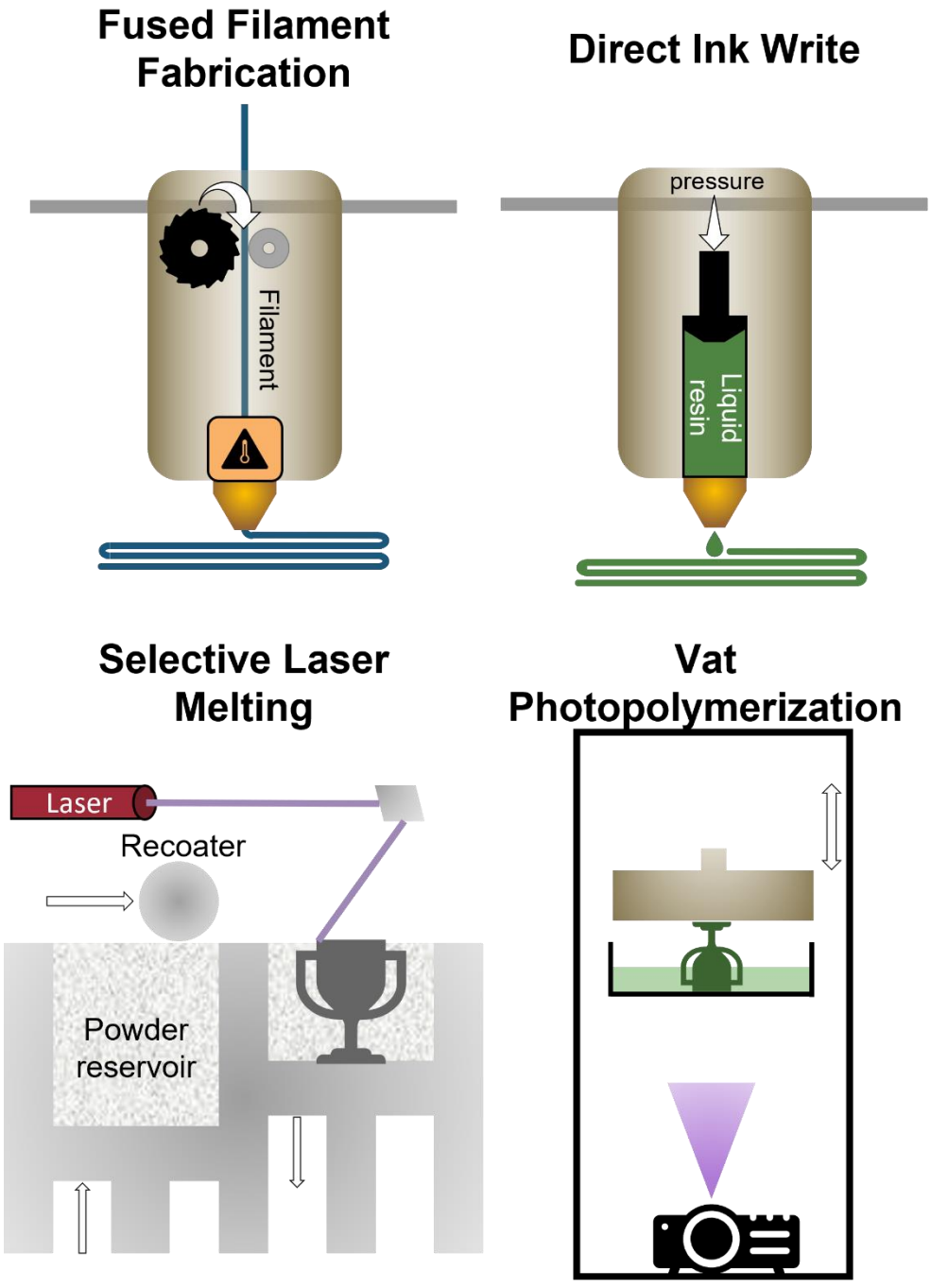

1.3.1 Vat Photopolymerization

Stereolithography (SLA), or more generally vat photopolymerization (VPP), is a subset of AM originally invented in the mid-1970s [37]. The first true stereolithography printer design was patented in 1986 by Charles Hull [38], who later founded 3D Systems. The process utilizes a laser to raster over a surface and selectively cure a photosensitive resin into a polymer of the desired cross-section. A variation of VPP is digital light processing, or DLP, which cures each layer by using a projector to display an image of the entire layer at once. Regardless of the light source, the process proceeds in a layer-by-layer fashion until the desired 3D object is formed. VPP offers very high resolution; high speed; minimal anisotropy, especially in the x-y plane; and low cost compared to other AM methods like fused filament fabrication, selective laser sintering, and material jetting [22, 26, 27, 39-41]. VPP is suited for many applications that require small runs of precise, custom parts, such as cell growth scaffolds, dental implants, microfluidic devices, prosthetics, and surgical simulations [42-45]. Vat photopolymerization printing offers benefits that are not available to traditional manufacturing, such as the ability to produce complex internal geometries, print single parts in multiple materials, and produce small quantities of one-off parts without the need for costly and time-consuming tooling or supply chain infrastructure. This capability has been explored in several case studies, including parts for the F-18 Super Hornet aircraft [29], LEAP jet engine parts at CFM International [30], aerospace brackets [31], and general aircraft components [32]. AM is therefore a promising alternative to traditional manufacturing beyond simply rapid prototyping.

Vat photopolymerization printer designs are largely unchanged from their initial design in the 1980s. A standard VPP printer consists of a build platform, a resin vat containing a photosensitive resin, a light source, and optionally a tilt or peel mechanism. To print using VPP, a CAD (computer-aided-design) model is loaded into a "slicer" program, which slices the 3D model into layers. Typical layer thicknesses are on the order of 25 to 150 microns, although some systems are capable of printing thicker layers. The minimum and maximum layer thicknesses achievable on a printer are also heavily dependent on the photopolymerization properties of the resin, which will be explored in subsequent sections. Figure 2 shows the progression from the original CAD model to 2D slices. The slicer program also generates toolpaths to control the motion of the various printer components, including moving the build platform up and down on the z-axis, triggering the laser or other light source, and executing a tilt or peel sequence. Most often, these toolpaths are written in a simple language called gcode that can call specific motors to move as needed. With the appropriate firmware installed on a microcontroller board, these human-readable commands can be translated into machine-readable commands, that ultimately result in motion. In laser-based SLA, the laser is controlled by two galvanometers, or galvos, that direct the light to the appropriate x- and y-coordinates. The peel mechanism is typically controlled by either lifting the z-axis, lateral motion, or tilting motion.

Figure 2

CAD Slicing Process

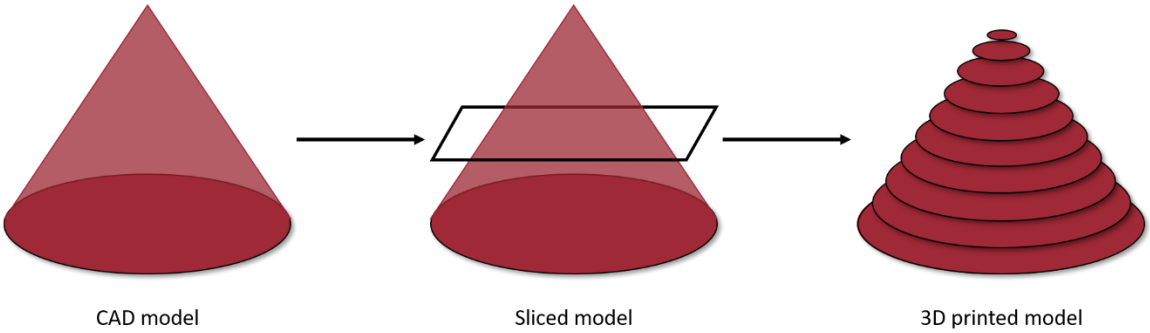

Vat photopolymerization printer designs can be either top-down or bottom-up, which refers to the location of the light source relative to the resin vat. Early VPP printers used top-down methods, which are ideal for fast, extremely accurate printing. Top-down designs cure the polymer just below the top surface of the resin and make use of oxygen inhibition of free-radical polymerization to maintain a thin layer of uncured resin on the top surface. The build platform containing the part is lowered into the vat as it is completed. There is no motion needed other than the downward motion of the build platform as the print proceeds, which makes this type of VPP extremely fast. However, top-down designs require that the resin level is always above the current print surface. These printers, therefore, require a large volume of resin (typically >1L) and are consequently not well suited to a research environment. Bottom-up printers, by contrast, project light upward onto the bottom of the resin vat and the build platform is raised as the print progresses. Figure 3 shows an example of a bottom-up printer design, which is

by far the most common modern configuration. Subsequent sections in this thesis will describe bottom-up configurations unless otherwise specified.

Figure 3

Bottom-Up Printer Schematic

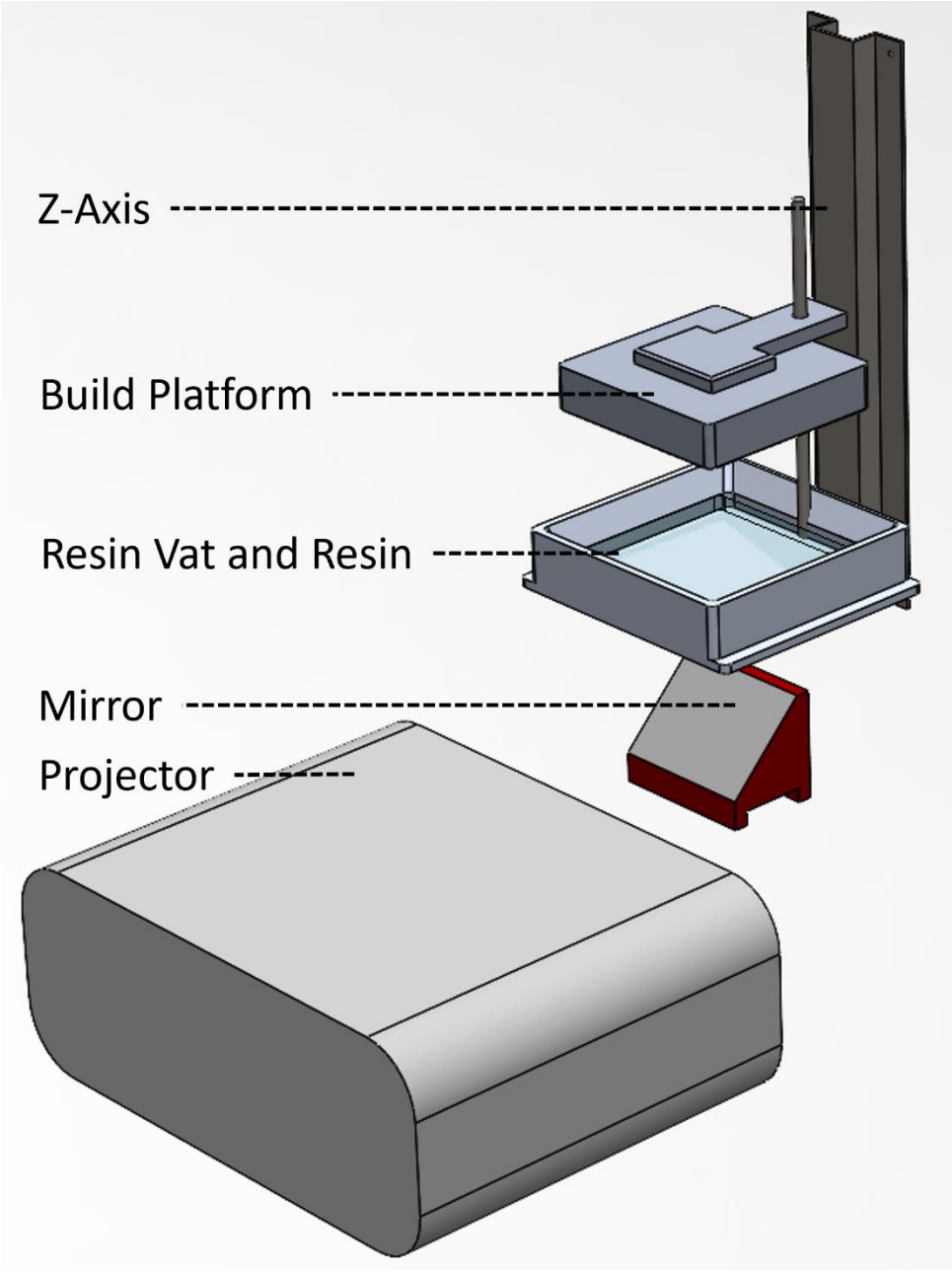

Typically, the bottom surface of a bottom-up resin vat is coated in an optically transparent, flexible material such as poly(dimethylsiloxane) (PDMS) or fluorinated ethylene propylene (FEP). Because the bottom of the vat is not in contact with air and is therefore not inhibited by oxygen, each layer cures directly to the bottom vat surface. Thus, a peel step is necessary after each layer to separate the cured polymer from the bottom vat surface. The peel step may entail either tilting the resin vat, moving the resin vat to the side while lifting the build platform, or simply lifting straight up. This peel step makes bottom-up designs slower than top-down, but the economical use of resin far outweighs the speed for most research applications.

The forces produced via the peel step are sometimes substantial enough to pull the in-progress print off the build platform. Use of a tilt or lateral motion in addition to lifting straight up with the build platform reduces some of the forces on the green-cured part, but these forces can still be quite high. Therefore, it is necessary to balance the percent conversion and the storage modulus of the polymer such that it is enough to hold its shape, but not so highly cured that it cannot be peeled off the vat bottom. Following the peel step, the build platform is lifted, and a layer of resin is redeposited either by swiping a wiper across the vat surface or by simply allowing the resin to flow back into place. The resin viscosity must be carefully tuned for bottom-up printer designs since the resin must be able to flow sufficiently quickly to re-coat the vat bottom. Printers that mechanically redeposit resin with a wiper or other mechanism can typically print resins with a higher viscosity than those that rely solely on flow. Following the print, post-curing of the "green cured" part is typically necessary to fully cure the polymer.

Digital light projection, or DLP, is a variation on the light source for VPP. There are many sub-variations of this technology, but at its simplest, a DLP printer uses a projector to expose each layer cross-section all at once, rather than rastering over the surface with a laser point to fill in the layer. This is typically achieved by "masking" a light source to form individual pixels, where a pattern of "on" and "off" pixels is overlaid on the light source to produce the desired shape. Liquid crystal display (LCD) masks are a low-cost masking option, but by far the most common masking technique is a digital micromirror display, or DMD. A DMD consists of an array of mirrors that can be directed towards the resin vat in the "on" state, or onto a heatsink in the "off" state. Light shines through the array, and "on" pixels are displayed and "off" pixels are dark. The light source could be monochromatic, as in a laser or LED, or a broad-spectrum light source, like a mercury vapor bulb. Each of the mirrors in the DMD correspond to a pixel in the image to be displayed. Use of a DMD enables very high resolution and image fidelity compared to other projection technology.

DLP printing has advantages and disadvantages compared to more traditional laser-based SLA. With a high-intensity light source, DLP can be much faster than SLA because each layer is exposed all at once, and the exposure time is the same regardless of the area to be exposed. In contrast, SLA printers must raster over the surface, which takes more time for very large exposure areas. Additionally, DLP printers are not susceptible to distortion at the edges of the resin vat. An SLA printer typically places the laser directly under the center of the resin vat (for bottom-up printers). Depending on the size of the resin vat, at the edges of the vat, the laser spot becomes more ellipsoid in shape which

can result in a loss of both accuracy and precision. This may manifest in the finished part as closing small holes in the part, loss of sharp edges, or other artifacts. By contrast, a DLP display is focused on the vat surface, and each pixel is mapped directly to the appropriate location in the vat. Pixels are only turned on or off and don't need to be directed at an angle to the appropriate location. DLP displays also can have a wide range of compatible light sources including both broad spectrum (i.e. mercury vapor bulb) or monochromatic (LED, laser). This means that a light source can generally be found to match price, safety, and material requirements. However, DLP systems are generally lower power compared to a typical laser for SLA (often by an order of magnitude or more) which may shift the exposure time needed to higher values. Ultimately, the print time is a result of the print area, resin photophysical behavior, light source type (whether broad-spectrum or monochromatic), masking type, and light source power.

1.3.2 Vat Photopolymerization Resins

The materials commercially used for VPP have not changed substantially since its advent in the 1980s. Commercial vat photopolymerization resins are typically comprised of acrylate or methacrylate oligomer(s), photoblocker(s), a photoinitiator, and colorant(s). Acrylates are by far the most common due to their increased reactivity relative to methacrylates, although methacrylates are also popular for their lower tendency to warp and better shelf stability. Table 1 lists the tensile strength (σ), Young's modulus (E), and heat deflection temperature (HDT) of selected commercial resins. Regardless of the resin chemistry, VPP printed parts are generally strong, have a fine surface finish, and have very strong interlayer adhesion compared to those made with other AM methods.

However, particularly for acrylate and methacrylate systems, volumetric shrinkage, warping, and lack of thermal stability limit the use of these resins in end-use parts, where parts produced with other manufacturing methods still outperform VPP products [41, 46, 47].

Table 1

Thermal and Mechanical Properties of Selected Commercial VPP Resins

	Resin	σ (MPa)	E (GPa)	HDT. @ 0.45 MPa (°C)
Formlabs [48]	Standard Series	65	2.8	73.1
	Grey Pro	61	2.6	77.5
	Rigid	75	4.1	88
	Tough	55.7	2.7	48.5
	Durable	31.8	1.26	43.3
	High Temp	58.3	2.8	120
3D Systems [49]	Accura 55 (Std and high res)	65.7	2.6	48.9-52.8
	White (Renshape 7810)	43.4	2.1	58.3
	High-Temp (Accura Bluestone)	66.9	9.7	267-284
	High Temp (Std) Accura PEAK	67.5	4.5	77.8
	High-Temp (VisiJet SL Hi-Temp)	66.0	3.4	57-110
Carbon 3D [50]	EPX 82 (Epoxy)	80	2.8	130
	RPU 70	40	1.7	60
	RPU 130 (Rigid Polyurethane)	35	0.9	120
	CE 221 (Cyanate Ester)	85	3.9	230
	UMA 90 (Urethane Methacrylate)	30	1.4	45

An early method for improving on the downsides of acrylate and methacrylate polymers is the use of epoxy materials, either instead of or in addition to the acrylate/methacrylate [51]. Epoxy resins have been used in composite fabrication for many decades due to their superior thermal and mechanical properties, low shrinkage during cure, chemical resistance, excellent adhesion to fillers and fibers, and toughness [4, 51]. However, photocuring of epoxy resins typically requires cationic photoinitiators (usually an aryl sulfonium or iodonium salt), which have a low curing speed and produce a polymer with very poor mechanical properties compared to thermally cured epoxies [4, 26, 51]. To mitigate these speed concerns, some groups have made use of oxetanes rather than epoxies, which exhibit similar mechanical properties but cure faster [46]. Another strategy is to include a free-radical photosensitizer in addition to the cationic photoinitiator [52, 53]. Diaryliodonium and triarylsulfonium salts do not absorb in the visible light region and so therefore cannot be initiated using visible light; UV light must be used instead, which is more energy-intensive and comes with safety concerns. The use of a free-radical photosensitizer enables use of low-intensity, visible light to initiate the curing reaction if a suitable photosensitizer is chosen. This approach substantially improves the speed of the photoinitiated curing reaction such that it is sufficiently fast for SLA printing, and allows for the use of low-intensity, visible light.

There are several requirements of a VPP resin beyond being photocurable. First, the resin must have a low enough viscosity to allow for the resin to flow back into the void left by the part when it is lifted off the vat surface. Typically for printers with a wiper or other resin deposition method, a viscosity of 10,000 cP at the printing

temperature is an acceptable upper limit [54, 55]. For use in printers without a resin deposition method (relying simply on flow to recoat the vat), 1000-2000 cP at the printing temperature is a more suitable upper limit [56]. Generally, resin viscosity should be tuned with reactive diluents to be as low as possible while still achieving the performance properties for the desired application.

In addition to viscosity requirements, a VPP resin must also cure fast enough for printing. One common way to evaluate curing behavior is through determination of the "working curve" parameters as developed by Jacobs [27]. This experiment provides the critical energy of curing (E_c) as well as the depth of penetration (D_p). In this experiment, a series of specimens are printed with varying energy "dose," which is a function of the light source power, laser speed (if applicable), and laser spot size (if applicable). These samples are printed without the build platform in place such that the thickness is not limited by the build platform. Instead, thickness builds up as a direct function of the dose applied to the resin. The thicknesses of each specimen are measured as a function of dose. The thickness is plotted against the log of the dose, and the model in Equation 1 is fit to the data. The x-intercept of the resulting plot is the critical energy dose, or the minimum energy required to cure the resin just to the point of solidification. The slope of the line gives the D_p, or the depth at which the light entering the resin is attenuated by 1/e [26, 27]. These two characteristic values, E_c and D_p, correspond roughly to the minimum energy dose needed to cure a layer and the maximum attainable layer height, respectively. These values are characteristic of the resin and are independent of the printing parameters.

$$C_d = D_p \ln \frac{E_{max}}{E_c} \quad (1)$$

Another common characterization method for VPP resins is by photorheology. The complex viscoelastic behavior of the resin as it cures into a polymer is evaluated as a function of shear rate for a given irradiance. The time at which the storage modulus crosses over the loss modulus is considered the minimum exposure time for the resin to go from liquid-like (higher loss modulus) to solid-like (higher storage modulus) at a given light source irradiance. With knowledge of the modulus crossover time and irradiance of the photorheometer light source, a critical energy dose can be determined, and exposure time (for DLP) or speed (for SLA) may be calculated from this dose value [57-61]. The utility of these experiments has been demonstrated by Hofstetter, et al. who have combined both working curve measurements and photorheology measurements to determine appropriate exposure time for a DLP resin [57]. Li et al also showed that the experimentally determined modulus crossover time can be used, along with absorbance of the liquid resin and the solid polymer, to predict working curve parameters, which showed good agreement with experimentally determined working curve values [58]. Additionally, the plateau value of the storage modulus may be used to evaluate if the resin will survive the peel forces in the peel step of a bottom-up printer. However, the utility of this value is still under investigation and has not been well-characterized.

1.3.3 Vat Photopolymerization Composites

At the time of this writing, there are no commercially available, fully-automated VPP printers that can place fiber reinforcements in-situ. However, composite resin systems, containing short chopped fibers or nanomaterials, have existed for many years.

Silica particles, especially nanosilica particles, are a popular reinforcing material for increasing the glass transition temperature, thermal stability, and mechanical properties [14, 16, 20, 23]. Various other types of nanomaterials are very common. Properties of these nanofilled resins include electrical conductivity with the use of silver nanoparticles, graphene, ceramics, or diamond/SiC [21, 62-66]; stiffness, strength, and cell growth promotion via the addition of hydroxyapatite or alumina particles [67-70]; stiffness, strength, thermal stability, and light weight through use of carbon nanotubes or carbon fibers [17, 71, 72]; and strength and thermal stability via the addition of glass fibers [12, 73, 74]. Woven glass fiber mats have been included in VPP prints, demonstrated by both Sano et al. [12] and Idrees et al. [74]. Both works demonstrate improved mechanical properties relative to the neat matrix. In particular, the work by Idrees demonstrates that the presence and size of resin-rich layers included in these composites are critically important for toughness and strength. However, both works place the mats using a hand-layup technique. The next logical step towards improving VPP part properties is, therefore, to automate the placement of mats to make these composites more industrially relevant.

1.4 Interpenetrating Polymer Networks

Interpenetrating polymer networks, or IPNs, are an industrially relevant class of polymers that provide enhanced mechanical properties compared to neat polymers. IPNs are comprised of two or more crosslinked polymers, at least one of which is made in the presence of the other [75, 76]. These differ from copolymers in that the different polymer networks are synthesized via different reaction mechanisms, although they may be

chemically linked depending on the specific chemistry and functionality of the monomers. The first synthesis of an IPN was performed in 1960 by Millar [76], consisting of styrene and divinylbenzene networks. There are generally two main types of IPN: simultaneous and sequential. Simultaneous IPNs are characterized by two or more networks being formed in the presence of each other, at the same time. In contrast, in a sequential IPN, each network is formed independently of the other(s) in discrete steps. For either type of IPN, the two or more polymer networks may be covalently bonded or simply intertwined. Acrylate- or methacrylate-epoxy IPNs, both sequential and simultaneous, have been well-characterized in the literature [46, 75, 77, 78]. For photocurable formulations, the (meth)acrylate network typically provides fast photocuring speed and holds the desired shape during a subsequent post-curing step. The epoxy monomers, crosslinker, and curing agent are held suspended in the (meth)acrylate network. The part is then fully cured using either heat alone or a combination of light and heat to further the conversion of both the (meth)acrylate and epoxy networks. A schematic representation of the sequential IPN process used in this work is shown in Figure 4.

Figure 4

IPN Curing Process Schematic

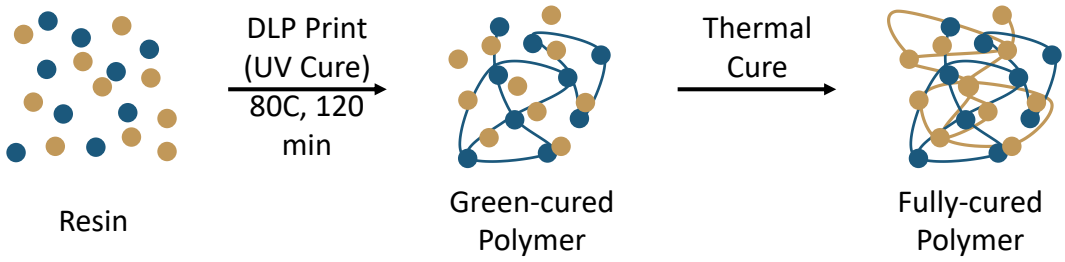

IPNs have been used extensively in VPP resins, and many examples are present both commercially and in peer-reviewed literature. Simultaneous IPN resin formulas have existed since the late 1980s in an attempt to address the shrinking and curling issues with early acrylate resin formulations [79-81]. Modern resin formulas are commonly comprised of either simultaneous or sequential IPN systems (most commonly acrylate-epoxy), and IPNs are offered by most of the modern 3D printing companies today. Carbon Inc. is an exceptional pioneer in this area, holding 9 patents since 2016 on dual-cure resin systems at the time of this writing [82-89]. In the literature, epoxy-acrylate/methacrylate systems [90-97] are by far the most common, but other chemistries such as silicone-epoxy [98] and cyanate ester-acrylate/bismaleimide [93, 99-101] are also represented. Use of an IPN resin system is a popular approach to improving the mechanical properties of VPP printed parts.

1.5 Thesis Summary

This thesis work describes the design and construction of an automated DLP composite printer for use in military applications. The addition of fiberglass

reinforcement material improves the mechanical properties of VPP printed parts with minimal loss of thermal properties. This printer design therefore shows promise as a means of manufacturing small runs of replacement or prototype parts, especially at the point of need for military use. More generally, this printer is intended as a tool for studying additively-manufactured fiber reinforced composites. Automation of this process enables studying materials with very high loading rates that would otherwise be cumbersome to produce by hand. These high fiber fraction composites will be more comparable to traditional composites that typically have loading rates of up to 70% by volume, which is not feasible with hand-placed fiber mats. This work also presents a proof of concept of VPP printed composites with hand-placed fiber mats, which show modest increases in glassy storage modulus and minimal loss of thermal properties compared to the neat matrix. An IPN resin system was chosen for this initial study to maximize interlayer adhesion and mitigate any fiber-matrix debonding. Woven glass fiber mats were chosen as the reinforcing material due to their industrial relevance, low cost, and transparency to UV and visible light. Chapter 1 introduces the context, need, and basic principles of VPP printing, printer designs, and materials properties. Chapter 2 describes the custom printer design, including early designs as well as the current design and prototype. Chapter 3 provides an overview of the characterization techniques used in this work to evaluate the exemplar IPN resin system. The results of this characterization and corresponding discussion are outlined in Chapter 4. Finally, Chapter 5 provides conclusions and recommendations for future work, both in characterizing printed parts as well as the printer design itself.

Chapter 2

Custom Printer Design

2.1 Overview

In order to produce additively manufactured composite parts, a custom digital light projection 3D printer was developed that can embed fiber mats in a thermoset matrix. The fiber handling component of the printer has undergone two main iterations, both of which will be described in this section. Prototype 1 was designed for aligned, post-drawn nanofiber mats, manufactured from either PAN or PCL nanofibers [102-104]. These fibers range in diameter from a few microns down to hundreds of nanometers, and thicknesses are adjustable depending on the spinning time. These polymers were chosen with pyrolysis in mind to ultimately produce aligned carbon fiber mats. Prototype 2 was designed for a commercially available 7 ½ oz. plain woven E-glass fiber mat purchased from Fibreglast (Brookville, OH, USA), sized with an all-purpose sizing appropriate for vinyl ester and epoxy resins.

2.2 Prototype 1

The schematic in Figure 5 shows the details of the initial design, Prototype 1. The printer's mechanical components consist of a build platform and z-axis (green), optically-transparent resin vat (blue), 4K projector and mirror (red), and movable frame (purple) containing two fiber frames (yellow). A full list of components is tabulated in Appendix B. The resin vat is equipped with a servo tilt motor, which lowers one side of the vat after each layer is printed. This motion breaks the adhesive forces between the just-cured layer and the bottom of the resin vat. This is necessary for resin systems that have

exceptionally high cured adhesion to the bottom of the vat and helps to minimize the forces associated with peeling the just-cured layer off the bottom of the vat. Such forces can sometimes be large enough to pull the in-progress part off the bottom of the build platform, so it is necessary to minimize these where possible.

Figure 5

Prototype 1 Schematic

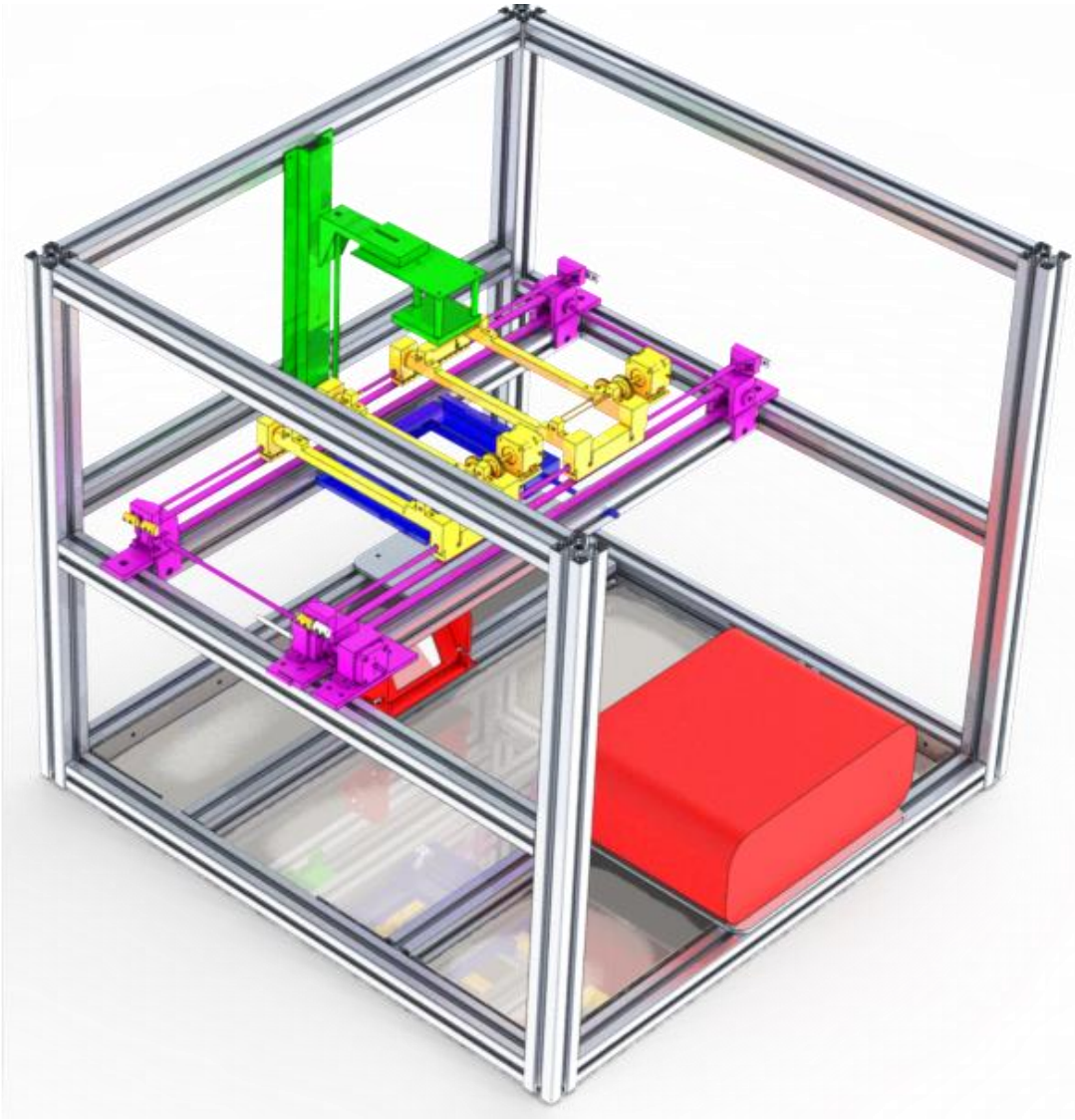

The printer utilizes a projector to illuminate a photocurable thermoset resin in a layer-by-layer fashion. This light source differs from that in most commercial designs. Typical SLA printers cure the resin via a laser, which rasters over the resin to selectively cure the desired cross-section. Lasers are fast, accurate, and are available in a range of

powers. The laser power can be tuned appropriately for a given resin to balance the cure time with warping and dimensional inaccuracies that can occur from over-curing. However, lasers require the use of galvanometers, which are responsible for tilting mirrors that direct the laser point to the appropriate location. There is currently no open-source software available that provides both the ability to control galvanometers and the option for custom code, which is essential for controlling the additional motors in the printer design. For this reason, we chose to utilize a digital light projection (DLP) design. DLP printers use a projected image to cure each layer in one pass. The DLP design permits the use of a powerful, free program called nanoDLP, which is highly adaptable compared to other slicing programs. NanoDLP offers the ability to write custom code to be executed at either the beginning or end of a layer (before or after the light cures a layer, respectively). This capability is crucial for fiber dispensing and frame positioning. Furthermore, DLP may be able to achieve higher print resolution in the x-y plane depending on the resolution of the projector. Features in the x-y plane can be no smaller than the spot size. For a typical SLA laser, the spot size is generally on the order of 50-150 microns.[26, 27] By comparison, a projector with 4k resolution (3840 x 2160 pixels, 16:9 aspect ratio) projected onto a 10 x 5.27 cm surface has a pixel (spot) size of approximately 25 microns. Very high resolution in the x-y plane is therefore achievable for small, highly detailed parts.

The location of the projector and mirror in the printer design are indicated in red in Figure 5. The 4k projector (BenQ HT2550) contains a mercury-vapor bulb, which offers a broad range emission ranging from UV-C up to the near-IR range. While the

mercury-vapor bulb has a lower irradiance compared to a laser, the broader light output allows for more flexibility in the choice of photoinitiator as well as resin chemistry. Resins that strongly absorb light at the output wavelength of a laser (typically 405 nm) are unsuitable for traditional VPP since they attenuate the light and limit its ability to activate the photoinitiator. However, these resins may be printable on a DLP printer, where there is some output in the UV as well as the visible range. The broad output of a mercury vapor bulb offers greater flexibility in choice of initiating wavelength, allowing exploration of a wider range of resin-photoinitiator systems.

The custom printer design deviates from existing printers in a few key areas. The primary difference is the addition of fiber frames, highlighted in yellow in Figure 5. Two frames were built such that fiber mats of opposing alignment (±45°) could be used. In this way, the mats could be placed in alternating alignments to maximize strength and minimize warping. The entire frame system is also controlled by a stepper motor and belt-and-pulley system to control lateral positioning, shown in purple in Figure 5. The lateral motion is needed so that the appropriate frame can be placed under the build platform for incorporation into the next layer. The inclusion of multiple frames allows for opposing fiber alignment, which is typically desirable for the best strength and minimal warping across the part [4].

To use the fiber system, spools of fibers are loaded into the frames. These spools are individually controlled by stepper motors attached to a spool pin. The fiber frame motion and positioning are controlled by a stepper motor and belt-and-pulley system, as indicated in purple in Figure 5. The frames are separated by an open space large enough

for the build platform to reach the resin vat and print normally. This opening maintains the ability to print without fibers, e.g. for rafts, support material, or regions of the part that do not require additional reinforcement. This feature conserves fibrous material and allows the printer to be used even if fibers are not required. For layers with fibers, the print proceeds as follows. First, the appropriate frame moves under the build platform at the beginning of the desired layer. The build platform will then lower and press the fibers into the resin. Next, the light illuminates the polymer in the appropriate shape to initiate curing. The cured layer is peeled off the bottom of the vat via a tilt mechanism, which breaks adhesion between the resin vat and the recently cured layer. After the peel step, the build platform lifts high enough that the fibers are detached from the fiber frame support, and the print will proceed as usual. Excess fibers on the edge of the print are trimmed in post-processing.

The printer control strategy is detailed in Figure 6. The printer is controlled by a free software program called nanoDLP, which is hosted on a Raspberry Pi 3B+. NanoDLP can be accessed from any browser that is connected to the same network as the Raspberry Pi. The Raspberry Pi is responsible for generating all movement commands and “slicing” a 3D model into 2D layers, as well as sending 2D sliced images to the projector. The movement commands are translated by the microcontroller board (Megatronics V3.0) to control the moving parts of the printer.

Figure 6

Printer Control Strategy

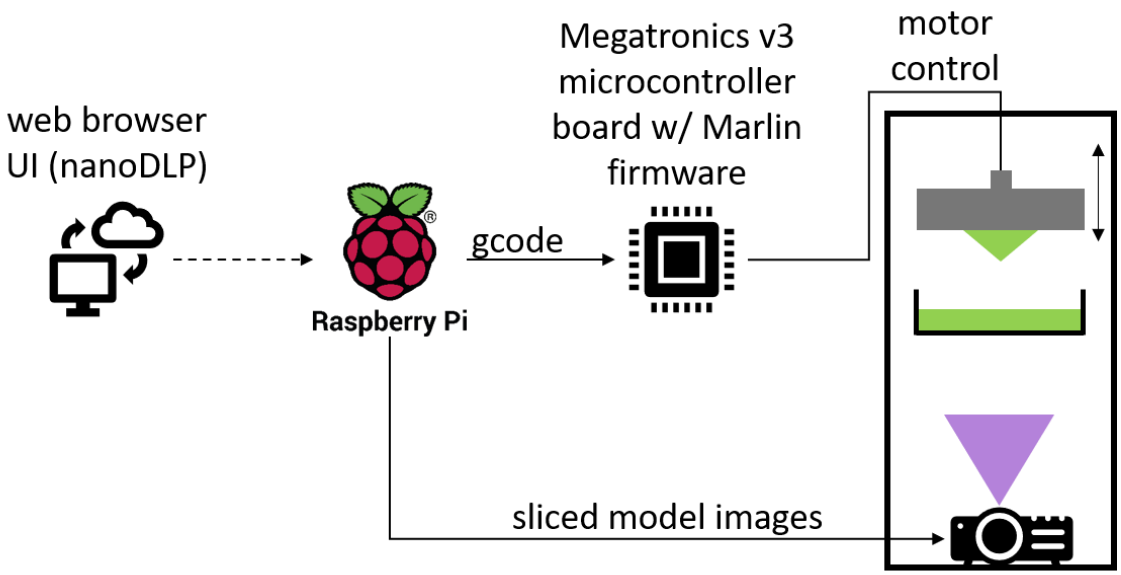

2.3 Prototype 2

This first prototype introduced the electronics, software, and mechanical components needed for a DLP composite printer. This design had a few flaws; namely, the many additional motors (two for each of the fiber frames, and one to move the fiber frames back and forth) and the lack of fiber feedstock flexibility. The feed-side spool pins in this design are located very close to the fiber frame itself, which leaves little room for full-size spools and limits scalability of the printing process. Additionally, the motor controlling fiber dispensing is attached directly to the spool pin. This means that the rotational distance traveled must change as the diameter of the spool changes, as the spools go from full to empty. This added additional complexity to the coding that was not

feasible in gcode. Furthermore, the fiber system was designed for a non-commercialized fiber feedstock, which introduced difficulties in feedstock consistency and access.

Several changes were made to the printer design to address these drawbacks. To improve on the feasibility and practicality of the design, we decided to move towards a commercial, woven fiber product. The fiber tape was pre-cut into perforated squares using a VersaLaser VL3.50 from Universal Laser Systems equipped with a 50W CO_2 laser, set to 30% power and 3.0% speed. The fiber cut-outs were perforated such that they held their shape on the roll but did not separate from the surrounding tape until after the printed layer was cured. This solved several problems. First, the fiber tapes are commercially available, so we were able to obtain fibers in any quantity needed. Second, as we moved to a traditional product containing fibers woven at 90° to each other, the need for a second fiber frame was eliminated. Each fiber layer contained fibers at both 0° and 90°, and there was no need to alternate between different fiber alignments. Additionally, we moved the motor controlling dispensing (termed the "velocity motor") in-line with the fiber tape, such that the fullness of the spool had no impact on how far the motor needed to rotate. This change significantly simplified the gcode needed; rather than needing to calculate a rotational distance based on the diameter of the spool at a given moment, a set amount could be dispensed each time (assuming consistent fiber mat spacing). To control the alignment and height of the fiber tape as it travels across the resin vat surface, a series of nip rollers were added. These rollers guide the tape and ensure it is planar with the resin vat when the fibers are pushed into the resin. Lastly, a torque motor was added to the tape system on the take-up side, after the resin vat. The

torque motor varies its shaft rotation (either clockwise or counterclockwise) in order to maintain a constant tension on the tape. The torque motor operates individually from the printer and is attached to a spindle, which turns to take up any slack in the tape. This motor keeps the tension on the tape constant as the velocity motor dispenses tape.

A schematic of Prototype 2 is shown in Figure 7. The tape travels up and over the velocity motor spindle, through a series of nip rollers, over the surface of the vat, through some additional nip rollers, and finally is taken up by the torque motor. The order of rollers through which the tape passes is indicated by the red arrows.

Figure 7

Schematic of Prototype 2 Showing Direction of Tape Travel

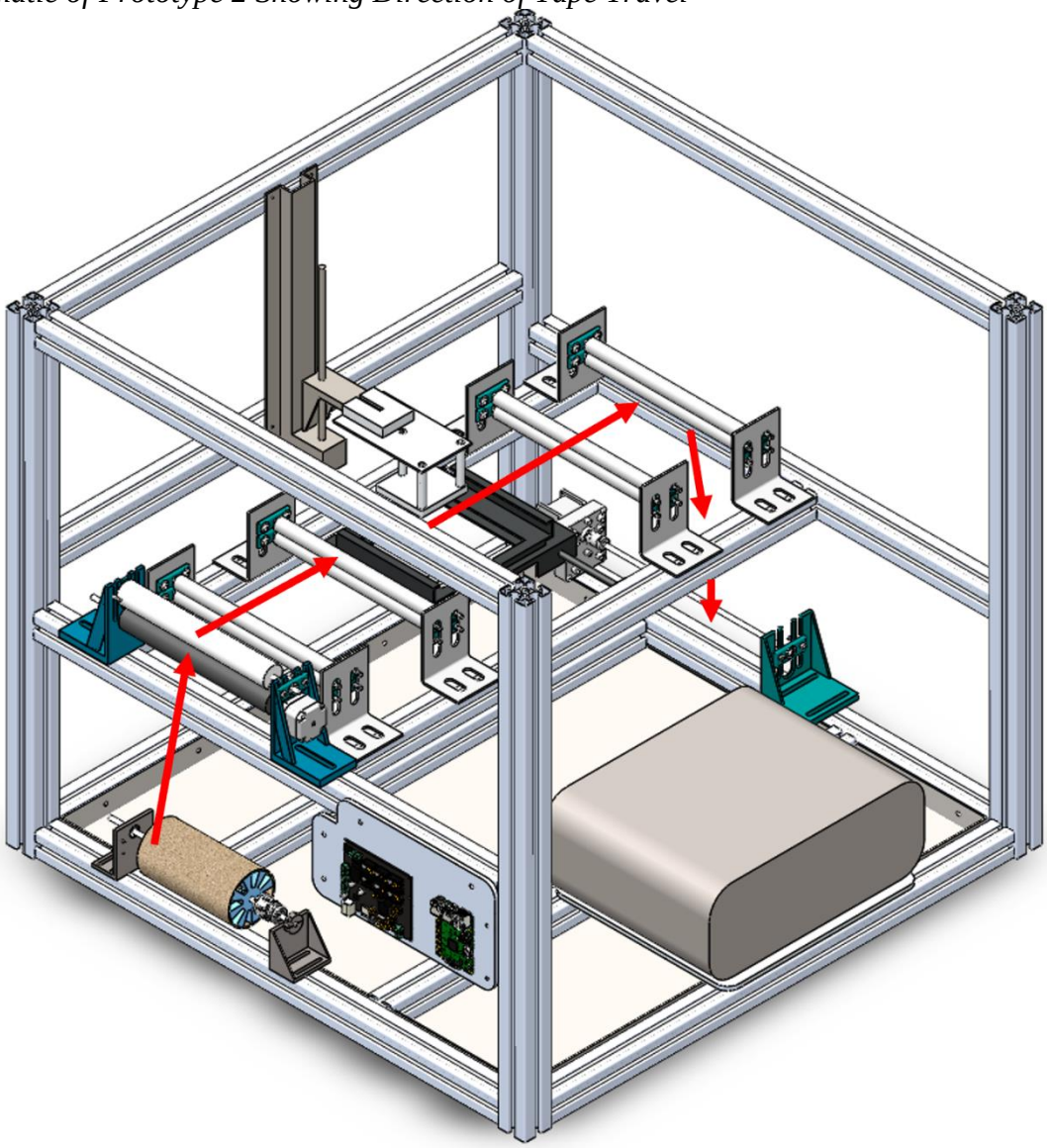

The printing process proceeds as follows: first, the tape is drawn through the tape handling system, which consists of the spool, velocity motor, nip rollers, and torque motor. The first perforated fiber square is then positioned directly under the build platform. Next, the build platform lowers into the vat, pressing the fibers into the resin and against the vat surface. Once all motions are completed, the projector is triggered, and the appropriate shape is projected onto the vat bottom to cure the resin. Then, the tilt motor is activated to peel the cured polymer off the vat surface. The build platform lifts, and the fibers remaining at the perforated edges are torn to release the fiber mat from the tape. Finally, the tape is advanced forward by the velocity motor, and the resulting slack in the tape is taken up by the torque motor.

Prototype 2 is a large improvement on Prototype 1. Prototype 2 makes use of commercial materials which are easily obtainable and relatively inexpensive. Additionally, Prototype 2 is more adaptable to spools of different size if needed. While the spool holder attached to the shaft was designed for the cardboard tubes on which the fiber tapes are packed, a range of spool holders could be designed to fit different spools. Prototype 2 also significantly simplifies the gcode required to control the printer by eliminating the need to dynamically calculate travel distances on the velocity motor. This leaves two spaces open on the board for additional motors or tools that may be needed for future iterations, e.g. an on-board laser cutter, post-printing curing lamp, etc. These potential added components will be described in Chapter 5. This printer was used to fabricate all printed parts described in subsequent chapters, although the fiber tape system was not used and fibers were instead hand-placed into the prints. A basic dispensing and

tape alignment test has also been performed, however, and it was found that the printer is able to adequately align cut squares with the bottom of the build platform. There are additional changes needed before a fully automated print test can be performed. The suggested changes are outlined in Chapter 5.

Chapter 3

Characterization and Experimental Methods

3.1 Introduction

The characterization methods, materials, and synthesis methods used within this body of work are described in the following chapter. The characterization techniques used for the polymers and printed composites are detailed. The synthesis and formulation of a sequential dual-cure IPN resin is detailed. The printing method used for making both the neat matrix and composite samples are described.

3.2 Matrix and Composite Properties

The following sections are intended to serve as a brief introduction to the characterization techniques used in this work and outline the experimental methods used for each characterization technique. Density measurements, Fourier-transform infrared (FTIR) spectroscopy, and dynamic mechanical analysis (DMA) are described, and general theory is provided for each within their respective sections.

3.2.1 Density Measurements

Density was determined for the matrix, fiber mats, and composites, and was used to calculate fiber weight fraction, fiber volume fraction, and void fraction in the composites. The density of all cured samples was taken prior to any further testing. Using a density kit, the measured density, ρ_m, of each specimen was determined according to Archimedes' principle:

$$\rho_m = \frac{Wt_{air} \times \rho_{fluid}}{Wt_{air} - Wt_{fluid}} \quad (2)$$

where ρ_{fluid} is the density of the fluid and Wt is the weight for each material in either air or fluid. Water was used as the fluid. Weight fraction, W_f, and volume fraction, V_f, of the fibers in the matrix were determined from the measured weights and densities:

$$W_f = \frac{Wt_{c,air} - Wt_{matrix,air}}{Wt_{matrix,air}} \tag{3}$$

$$V_f = \frac{W_f / \rho_{fiber}}{W_f / \rho_{fiber,m} + (1 - W_f) / \rho_{matrix,m}} \tag{4}$$

where $Wt_{c,air}$ is the weight of the composite in air, $Wt_{matrix,air}$ is the weight of the matrix in air, $\rho_{fiber,m}$ is the density of the fiber mats, and $\rho_{matrix,m}$ is the measured density of the matrix.

In order to calculate void fraction in the composites, the theoretical density was first computed. Theoretical density of the composites, $\rho_{c,t}$, was determined from fiber density, matrix density, and volume fraction according to:

$$\rho_{c,t} = \rho_{matrix,m} \times (1 - V_f) + \rho_{fiber,m}(V_f) \tag{5}$$

and void volume fraction, V_0, in the composites was computed according to:

$$V_0 = \frac{\rho_{c,t} - \rho_{c,m}}{\rho_{c,t}} \tag{6}$$

where $\rho_{c,m}$ is the measured density of the composite.

3.2.2 Fourier-Transform Infrared Spectroscopy

Fourier-transform infrared spectroscopy (FTIR) is a type of absorption spectroscopy that provides information about molecular rotations and vibrations. FTIR measurements are fast, sensitive, and nondestructive, which makes FTIR a popular

technique for analyzing both organic and inorganic compounds. The IR spectrum is typically divided into near (12,800-4000 cm^{-1}), mid (4000-200 cm^{-1}), and far (200-10 cm^{-1}) regions [105]. The mid-IR region is most commonly used for both quantitative and qualitative analysis, since most organic materials will exhibit a fundamental vibration somewhere in this region. Near-IR is also used for quantitative analysis, although less commonly. Absorption bands in the near-IR are overtones or combinations of fundamental stretching vibrations that occur in the fingerprint region of mid-IR (3000-1700 cm^{-1}) [105]. Far-IR spectroscopy is typically reserved for inorganic molecules, where the vibrations between metal atoms and ligands happens at very low frequencies (>650 cm^{-1}). Far-IR can also be used to evaluate rotational transitions in the gas phase [105]. Both the mid- and near-IR regions are used for quantifying extent of cure in the field of polymers.

A molecular vibration or rotation is active in the IR region if it undergoes a net change in dipole moment. If the frequency of the radiation exactly matches the natural vibration frequency of a molecule (or functional group), the radiation is absorbed. These absorptions are highly characteristic of specific functional groups, which make FTIR suitable for qualitative identification in addition to quantitative analysis. Some types of molecular vibrations are shown in Figure 8.

Figure 8

Types of Molecular Vibrations

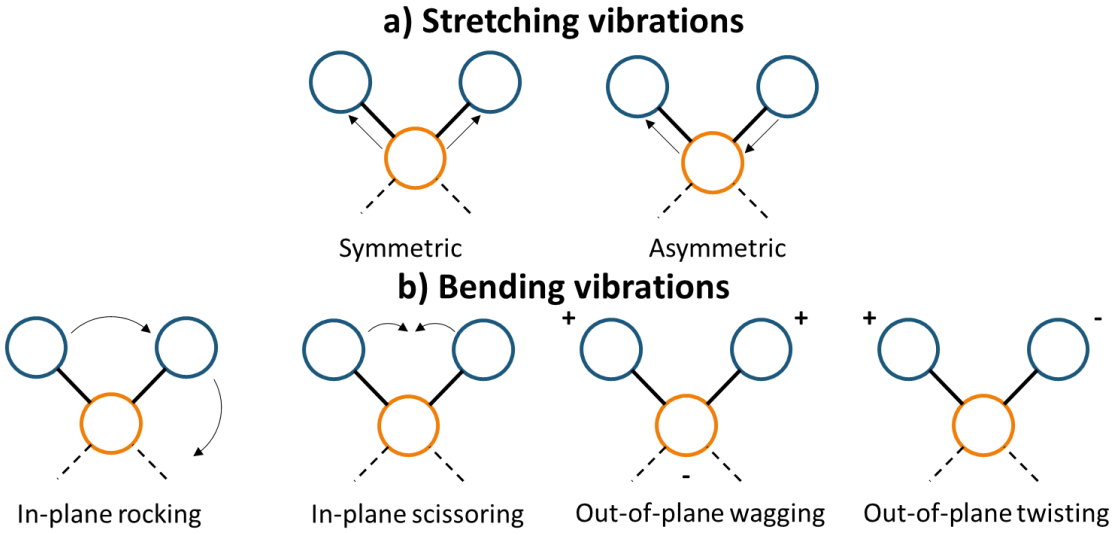

Typically, FTIR instruments collect signals in the form of percent or fraction of transmission, which can be converted to absorbance values. The resulting absorbance values are linear with concentration according to the Beer-Lambert Law,

$$A = \varepsilon l c \tag{7}$$

where ε is the extinction coefficient at a given wavelength, l is the path length, and c is the concentration. This allows for use of absorbance values to calculate relative concentrations, as in extent of cure calculations for polymers [106].

FTIR instruments collect data in the time domain and convert the data to the frequency domain through a Fourier transform. This is accomplished using a Michelson interferometer, which allows for collection of very high-frequency signals such as those in optical spectroscopy. In a Michelson interferometer, a beam of light impinges on a

beamsplitter, which reflects half the radiation and transmits the other half. The twin beams are then each directed at a mirror, one of which is moveable and one of which is fixed. The beams then hit the beamsplitter a second time, and half of each beam is directed towards either the sample and detector or back to the radiation source. The motion of the moveable mirror causes a difference in path length, which is related to time. As the light travels through the sample, the sample absorbs light at frequencies that perfectly match that of a molecular vibration, and the light impinging on the detector is reduced in intensity compared to the source. The result of this process is therefore a plot of intensity as a function of time, called an interferogram. The time-domain interferogram is converted to a frequency-domain spectrum through mathematical transformation.

FTIR instruments can be of the single-beam or double-beam type. In a single-beam instrument, the reference or background spectrum is collected separately from the sample. The ratio between the two signals is computed to give the transmittance at each frequency. In a double-beam instrument, the sample and reference signals are collected simultaneously, such that data is obtained at each mirror position. This design compensates for source and detector drifts as well as any changes in atmospheric conditions. Generally, a single-beam instrument is sufficient for routine sample testing.

In this work, a single-beam FTIR instrument (Nicolet iS50) was used in the near-IR region to determine extent of cure of polymers, utilizing a CaF_2 beam splitter. Three replicates from the same print (build platform) were collected for each test condition. Spectra were collected at a resolution of 2 cm^{-1} and 32 cumulative scans in the range of 4000-10,000 cm^{-1}, and a background spectrum was collected prior to each sample scan.

In this range, there are absorption bands characteristic of the C=C double bond stretch of the methacrylate at ~6165 cm^{-1} [107], N—H stretching and bending of the amine at ~5050 cm^{-1} [106, 107], and N—H stretching overtones of both primary and secondary amines at ~6675 cm^{-1} [106, 107]. The oxirane combination bending and stretching band at ~4530 cm^{-1} was not used in this study due to insufficient resolution of the peaks in this area of the spectrum; however, deconvolution of the spectrum would allow for quantitation of this peak.

Conversion was calculated for both the methacrylate and amine groups to determine the extent of cure for the methacrylate and epoxy-amine networks, respectively. Peak area absorbance values for the appropriate peaks for each network were collected for both the resin and polymers, and normalized against an internal standard, namely a peak for a vibration that does not participate in polymerization (C—H_2 at 5985 cm^{-1}) [107]. This normalization accounts for any differences in sample thickness (path length) or refractive index that impact the absorption area. Because there are two relevant peaks for the conversion of the epoxy-amine network, these peaks were averaged together to obtain an average amine conversion. Conversion of the methacrylate network, $\alpha_{methacrylate}$, and the epoxy-amine network, α_{amine}, were calculated according to Equations 8 and 9, respectively:

$$\alpha_{methacrylate} = \frac{\left(\frac{A_{6165\ cm^{-1}}}{A_{5985\ cm^{-1}}}\right)_{resin} - \left(\frac{A_{6165\ cm^{-1}}}{A_{5985\ cm^{-1}}}\right)_{polymer}}{\left(\frac{A_{6165\ cm^{-1}}}{A_{5985\ cm^{-1}}}\right)_{polymer}} \quad (8)$$

$$\alpha_{amine} = \frac{\left(\frac{A_{5050\ cm^{-1}} + A_{6675\ cm^{-1}}/2}{A_{5985\ cm^{-1}}}\right)_{resin} - \left(\frac{A_{5050\ cm^{-1}} + A_{6675\ cm^{-1}}/2}{A_{5985\ cm^{-1}}}\right)_{polymer}}{\left(\frac{A_{5050\ cm^{-1}} + A_{6675\ cm^{-1}}/2}{A_{5985\ cm^{-1}}}\right)_{polymer}} \quad (9)$$

These conversion values were determined at each step of the printing process, comprising the additive manufacturing step (AM), Form Cure step (FC), and post cure step (PC). These steps are described in greater detail in subsequent sections.

3.2.3 Dynamic Mechanical Analysis

Dynamic mechanical analysis, or DMA, is a powerful thermomechanical technique that gives information about the viscoelastic behavior of a material [108]. An oscillating (sinusoidal) deformation is applied to the sample (either strain- or stress-controlled, but most commonly stress-controlled), and the response of the sample to the deformation is measured. The phase angle or lag between the force and the resulting displacement, denoted δ, is measured as a function of temperature. This phase angle is 0° for a perfectly elastic material and 90° for a perfectly viscous material. For polymers, which generally exhibit both elastic and viscous behavior, the phase angle δ is between 0° and 90°. This value, as well as the material response to deformation, can provide information about damping, stiffness, elasticity, glass transition temperature (T_g), relaxation temperatures, cure or vitrification behavior, stress-relaxation behavior, and creep behavior as a function of time, temperature, and frequency of oscillation [108, 109].

Modulus values give information about a material's resistance to deformation, or stiffness. Modulus is defined as the slope of the stress-strain curve:

$$E = \frac{\sigma}{\varepsilon} \tag{10}$$

However, for DMA measurements, the complex modulus must be considered, due to the sinusoidal nature of the applied stress. The complex modulus provides both the storage modulus, or ability to return or store energy, (E') and loss modulus, or the ability to lose energy (E'').

$$E^* = E' + iE'' \tag{11}$$

These are derived from the complex stress and strain. Stress (σ) and strain (ε) are defined by the following equations:

$$\sigma = \sigma_0 \sin(t\omega + \delta) \tag{12}$$

$$\varepsilon = \varepsilon_0 \sin(t\omega) \tag{13}$$

where ω is the oscillation frequency, t is time, and δ is the phase angle. And E'(storage modulus) and E''(loss modulus) are defined by:

$$E' = \frac{\sigma_0}{\varepsilon_0} \cos\delta \tag{14}$$

$$E'' = \frac{\sigma_0}{\varepsilon_0} \sin\delta \tag{15}$$

The ratio of these two moduli gives the tan δ:

$$\frac{E'}{E''} = \frac{\sin\delta}{\cos\delta} = \tan\delta \tag{16}$$

The value of tan δ provides a measure of energy dissipation in a material under cyclic load. The glass transition temperature of polymers is often reported as the peak of the tan

δ curve. This corresponds with a large drop in the storage modulus as the material goes from a rigid solid to a more rubbery material.

Generally, a DMA experiment proceeds as follows. A thin (1.5-3 mm thick) bar of the material of interest is subjected to a sinusoidal deformation, or stress (σ), and the resulting strain (ε) is measured as a function of time, temperature, and frequency. The material's resistance to deformation is related to its modulus (E). The clamping geometry varies depending on the type of sample being tested and the desired information. For this work, a single-cantilever geometry was used, which is the preferred geometry for characterizing materials through the glass transition [109]. In this geometry, one end of the sample is kept fixed, while the other oscillates up and down according to a specified amplitude. Typically, the output of a DMA test is given as a plot of E', E'', and tan δ as a function of temperature. The tan δ value provides information about damping and energy dissipation during the test, while the temperature value at which the peak of the tan δ occurs is commonly reported as the T_g.

In this work, DMA thermograms were collected for both the neat matrix and composite samples on a TA Instruments Q800 DMA. A single cantilever geometry was used with sample size 2.5 x 12 x 35 mm^3. Samples were clamped using a torque wrench to a torque value of 7.5 in-lb. Tests were conducted at a frequency of 1 Hz and Poisson's ratio of 0.35, and deflection amplitude of oscillation of 7.5 μm. Samples were equilibrated at 0 °C, held isothermally for 5 min, then ramped at 2°C/min to 250 °C. For this work, all glass transition temperatures are reported as the peak of the tan δ curve, and

the glassy storage modulus is given as the E' value at 25 °C. Data was collected in triplicate using three different samples from the same print (build platform).

3.3 Materials

Phenol (99.5%) and 4-dimethylaminopyridine (DMAP) (99%) were purchased from Acros Organics (Fair Lawn, NJ, USA). Methacrylic anhydride (94%) was purchased from Alfa Aesar (Haverhill, MA, USA). Diphenyl (2,4,5-trimethylbenzoyl)phosphine oxide (TPO) was purchased from TCI (Tokyo, Japan). Isopropyl alcohol (IPA) was purchased from VWR (Radnor, PA, USA). Compressed nitrogen (N_2, 99.998%) and compressed argon (Ar, 99.999%) were purchased from Airgas (Radnor, PA, USA). Epon Resin 828 (diglycidyl ether of bisphenol A, Epon828) and diethyl toluene diamine (Epikure Curing Agent W) were obtained from Hexion (Columbus, OH, USA). Fabric style 120, 3 oz. E-glass woven fabrics were purchased from Fibreglast (Brookville, OH, USA). All chemicals were used as received.

3.4 Synthesis of PM-EM828

The resin was synthesized via a one-pot two-step reaction methodology as shown in Figure 9 [90, 110]. In a three-neck round bottom flask equipped with a mechanical mixer, phenol (75.00 g) and DMAP (4.92 g) were added. The mixture was purged with argon for 10 min and then methacrylic anhydride (124.09 g) was added. The reaction mixture was heated to 50–55 °C with continuous stirring. After 72 h, the reaction mixture was cooled to room temperature and a stoichiometric amount of Epon 828 (301.84 g) was added to the reaction flask. The mixture was then heated to 80 °C and monitored via acid number titration until a free acid number below 10 was obtained, corresponding to less

than 3% remaining acid. The resulting reaction vessel contained a mixture of phenyl methacrylate monomer (PM) and partially methacrylated Epon 828 (EM828) in a 1:1 mol ratio as well as minimal amounts of unreacted starting materials and dimethacrylated Epon 828.

Figure 9

Synthetic Scheme for Synthesis of PM-EM828 Resin

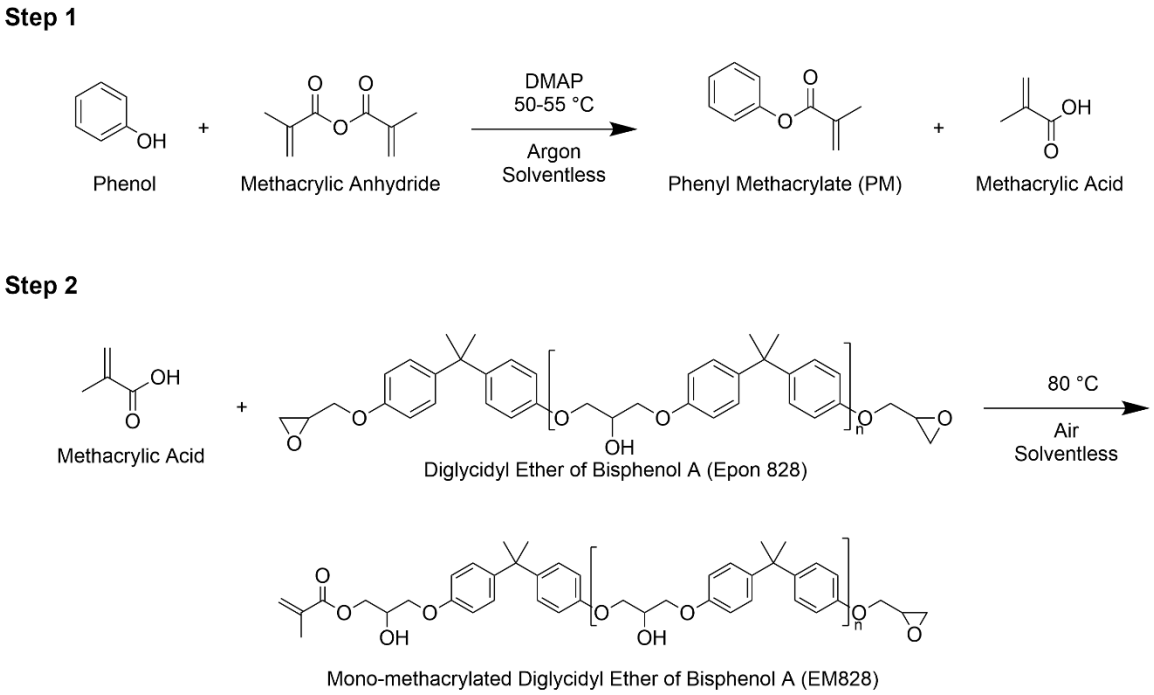

3.5 Formulation of PM-EM828

PM-EM828 resin was formulated via the addition of appropriate curing agents to the resulting reaction mixture, namely, TPO for the methacrylate network and Epikure W curing agent for the amine network. TPO was added to the reaction mixture at 2 wt% of the total reaction mixture, and a stoichiometric amount of Epikure W was added

assuming 100% conversion to EM-828 in the second step. These components were mixed in a Thinky ARE-310 planetary mixer for 10 minutes on a mixing cycle at 2000 rpm and 5 minutes on a defoaming cycle at 2200 rpm. These two mixing/defoaming steps were repeated once more for a total of 30 min mixing time.

3.6 Printing PM-EM828 and Composites

The Prototype 2 custom printer was used to fabricate all specimens in this study. The formulated PM-EM828 resin was added to an FEP resin vat. Depending on the desired layer height, 45 s (100 μm), 70 s (200 μm), or 90 s (300 μm) exposure time was used for each layer. The printed DMA specimens were arranged as in Figure 10. on the build platform for printing. For all flat-printed samples, the build platform was covered in aluminum foil held in place with double-sided tape to aid in specimen removal.

Figure 10

Arrangements of Printed DMA Bars on the Build Platform, a) Flat and b) Edge

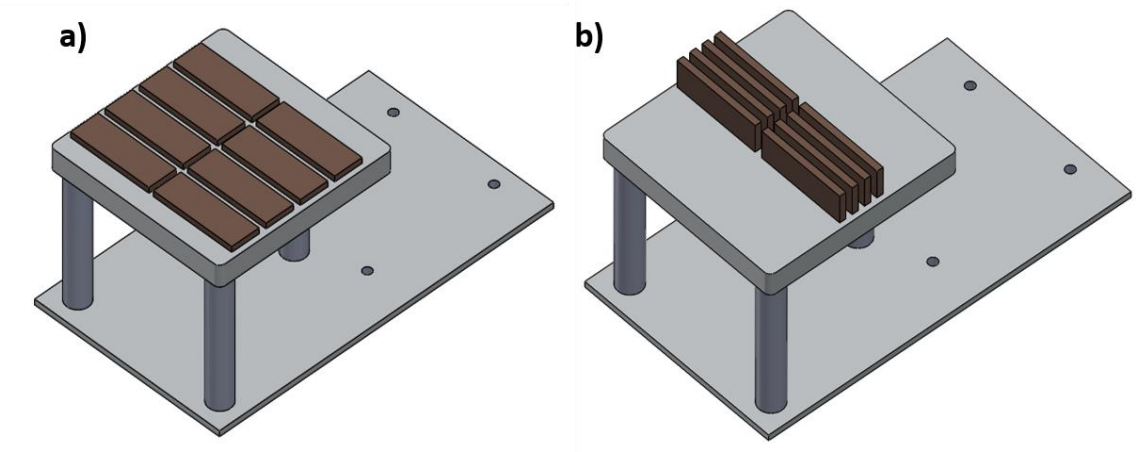

The exposure times for each layer height were determined through a ladder cure study as follows. Specimens were printed at the desired layer height beginning at 10 s exposure time for each layer. The print was then evaluated to determine answers to the following questions: (1) Did a solid form? (2) Is the solid stiff enough to hold its shape as it is removed from the build platform? (3) Is it able to be removed from the build platform? If the answer to (1) was no, the cure time was increased by 10 s and the test was repeated. Once a solid was formed, the cure time was increased by 10 s in increments until it was stiff enough that the answer to question 2 was yes. If at any point the answer to (3) was no, the cure time was reduced by 5 s until it was able to be removed. In this way, the exposure times for each layer height were determined systematically.

For printing of composites, pauses at the desired intervals were added via the nanoDLP software. Upon pausing, the build platform was removed, and fiber mats were placed by hand onto the previously printed layers. Fiber mats were trimmed to fit the perimeter of all printed samples. Mats were smoothed by hand to minimize the presence of bubbles and ensure sufficient wetting. After addition of the fiber mats, the build platform was returned to the printer, and the print was resumed. Upon completion of the print, the samples were removed from the build platform, and samples were washed in a Formlabs Form Wash containing isopropanol for 30 min, followed by 1 hr drying time. To further the conversion of both the methacrylate and epoxy networks, the dried samples were then postcured in a preheated Formlabs Form Cure (denoted FC) for 2 hr at 80 °C and 39W 405 nm light. Samples were allowed to cool ambiently to room temperature. Finally, the samples were postcured in a preheated thermal oven at 180 °C for 2 hr

(denoted PC). After postcuring, excess fibers were trimmed from the edges of the DMA bars using scissors. Any remaining fibers were trimmed using a razor blade.

Composites were fabricated containing fibers in every 4th layer (25% fiber-containing layers, or FL) at a 200 μm layer height. Samples were printed both flat and on edge using a 70 s exposure time. For the edge-printed samples, an additional set was fabricated using a 90 s exposure time to evaluate the effect of cure time on the resulting composite properties.

Chapter 4

Results and Discussion

4.1 Introduction

The main objectives of this work were to evaluate the effect of layer height and orientation (flat or edge) on extent of cure and DMA properties, as well as to demonstrate the feasibility of producing fiber-reinforced polymer composites on the custom DLP printer. To do so, a custom dual-cure sequential IPN resin, PM-EM828, was used in conjunction with woven glass fiber mats to fabricate composites. PM-EM828 contains both methacrylate (light-cured) and epoxy (thermally-cured) components, which make it an IPN. These are cured sequentially, where the methacrylate network is cured first in the additive manufacturing (AM) step, and the epoxy-amine network is cured second in a thermal post cure. These two networks are covalently linked together via the dual-functional crosslinker, EM828, which contains both methacrylate and epoxy moieties. PM-EM828 was chosen for its high thermal and mechanical properties, with a glass transition temperature approaching 140 °C and storage modulus as high as 3.2 GPa [90]. PM-EM828 also has a viscosity of approx. 1200 cP at 25 °C, well within the processable range for vat photopolymerization and low enough for fiber wet-out. The printed composites were evaluated for density, volume fraction, void fraction, extent of cure, storage modulus at room temperature, and glass transition temperature via the peak of the tan δ curve.

4.2 Printing PM-EM828 and Composites

Matrix samples were printed at a range of layer heights (100, 200, and 300 μm). Samples with a 200 μm layer height were printed in both flat and edge orientations. Composites were printed using a layer height of 200 μm, and both flat and edge orientations. Mats were carefully placed by hand such that one fiber orientation was parallel to the long dimension of the DMA bar. Exemplar trimmed and untrimmed edge-printed AM samples are shown in Figure 11. Some evidence of fiber pull-out is visible in the trimmed sample, particularly at the ends of the bar. However, good fiber wet-out was generally achieved, especially in flat printed samples.

Two different exposure times were evaluated for the edge-printed composite (70 and 90 s). The composite was first printed using the same cure time as the matrix, 70 s. Significant adhesive failure was evident in the edge-printed sample after the DMA test. It was hypothesized that the fiber-matrix debonding evident in these samples could be mitigated by increasing the exposure time and, consequently, increasing the initial AM extent of cure. However, similar failure was found in the samples cured for 90 s. We can therefore conclude that the failure is a result of the fiber mat orientation relative to the plane of the DMA test, and that orientation is critically important for parts that will be exposed to temperatures approaching 250 °C as in the DMA test.

Figure 11

Photographs of Printed Composites

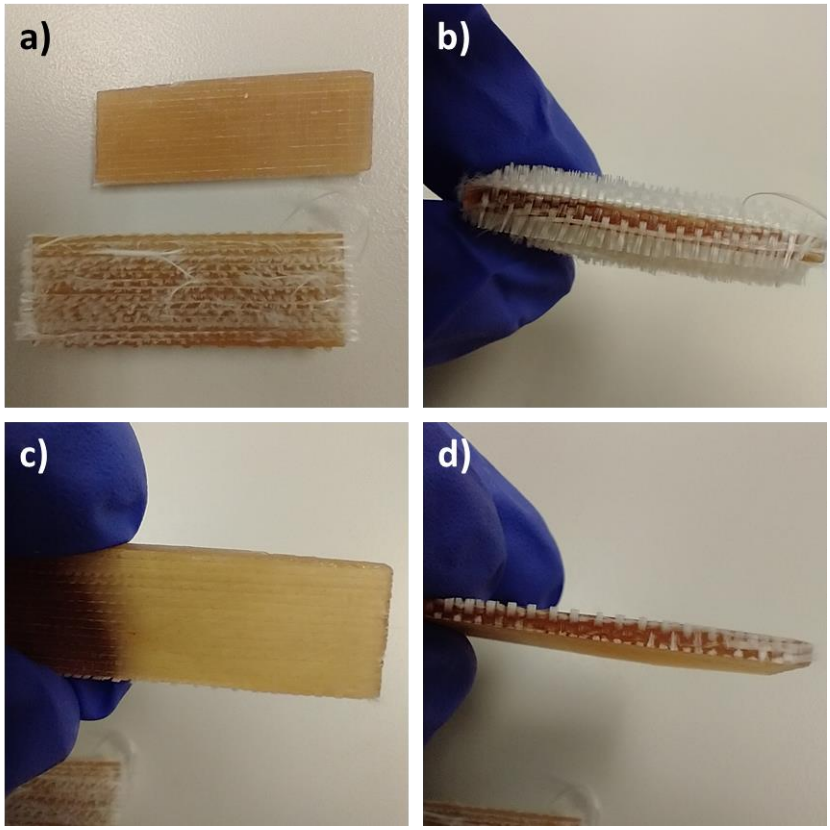

4.3 Matrix and Composite Properties

4.3.1 Density

Density measurements were collected for matrix samples at 100, 200, and 300 μm layer height, as well as for all composites produced by a colleague in the laboratory. The fiber weight fraction, fiber volume fraction, and void fraction were calculated for all composites from measured (experimental) densities. The results of these measurements are reported in Table 2. The density of the matrix was measured to be 1.201 ± 0.0076 g/cm^3 and the density of the fiber mats was measured to be 2.25 ± 0.15 g/cm^3 based on

Archimedes' principle. The matrix value is comparable to what has been previously reported in the literature (1.199 ± 0.003 g/cm^3) [90].

Table 2

Density Properties for Composites

Sample	Measured Density (g/cm^3)	Fiber Weight Fraction (%)	Fiber Volume Fraction (%)	Void Fraction (%)
25% FL, flat	1.257 ± 0.0024	10.47 ± 0.86	5.91 ± 0.51	0.97 ± 0.51
25% FL, edge, 70 s	1.250 ± 0.0047	10.76 ± 1.97	6.1 ± 1.2	1.74 ± 0.67
25% FL, edge, 90 s	1.252 ± 0.0012	8.24 ± 0.47	4.60 ± 0.27	0.43 ± 0.24

Overall, the densities of the composites are roughly the same. This is expected since the composites were all fabricated using the same fiber loading (same number of FL). The slightly lower fiber weight/volume fractions in the 25% FL, edge, 90s exposure samples are likely due to fiber pull-out in the trimming step. The edge-printed specimens have a large surface area perpendicular to the plane of the fiber mat, such that the ends of the fibers protrude from the flat plane of the specimen. The resulting large surface area makes trimming difficult and makes fiber pull-out likely. However, the void fraction of this sample is also the lowest of all the composites fabricated. Further investigation is needed to determine if this is a function of the longer cure time, fiber pull-out, or simply

within error of the density measurement. These results, however, suggest that parts printed on the custom printer should be carefully oriented to place areas with the highest surface area in-plane with the fiber mats.

The fiber weight fraction and corresponding volume fraction are quite low compared to typical fiber loading for industrially manufactured composites (50-70%) [4]. However, even at modest fiber loading of about 10% by weight (~5% volume fraction), the glassy storage modulus via DMA was increased from approximately 2.9 GPa to 3.7 GPa. This indicates that even small amounts of fiber have a strong impact on the resulting properties. These results also indicate that placing fibers in every layer, as in the custom printer, will likely offer dramatic improvements in strength, modulus, and toughness relative to the neat matrix. These DMA results are described further in Section 4.3.3.

The printed composites exhibit void fractions in the range of 0.43 ± 0.24 and 1.74 ± 0.67%. A review of recent epoxy-glass fiber composites where void fraction was reported suggest these void fraction values are on par or better than other composite fabrication methods, which show void fractions in the range of 0.5 – 5% [111-114]. The void fraction obtained will be a strong function of fiber weave, fiber material, fiber sizing, and resin viscosity. This particular combination of a medium-viscosity resin and satin-weave glass fiber mats, however, yields few defects in the form of voids.

4.3.2 Extent of Cure

Fourier-transform infrared spectroscopy was employed to measure the extent of cure, or conversion, of all polymer specimens fabricated. Extent of cure for the methacrylate network was determined after the additive manufacturing step (AM), Form

Cure UV-postcure (FC), and thermal postcure (PC) steps. Extent of cure of the epoxy-amine network was determined via conversion of both primary and secondary amines after the FC and PC steps, as it has been shown previously that there is no epoxy conversion for PM-EM828 during the additive manufacturing step [90].

Figure 12 shows an exemplar series of FTIR spectra for the neat matrix through the course of printing and postprocessing steps. Spectra are attenuated to 4500-9000 cm^{-1} to eliminate noisy regions outside of the main spectral area. Spectra are offset for clarity. All other FTIR spectra are shown in Appendix A. As the printing and post-curing process proceeds, the peak corresponding to the methacrylate C=C stretch at 6165 cm^{-1} decreases as the C=C double bond is converted to a C—C single bond as a result of polymerization. Similarly, the primary and secondary amine peaks centered at 5050 and 6675 cm^{-1} decrease as the amine groups are converted to tertiary amines in the epoxy network. Additionally, the band at 7000 cm^{-1} corresponding to O—H overtones grows in as the oxirane group ring-opens to form a hydroxyl in the FC and PC steps.

Figure 12

Exemplar Normalized FTIR Spectra For 100 μm Matrix

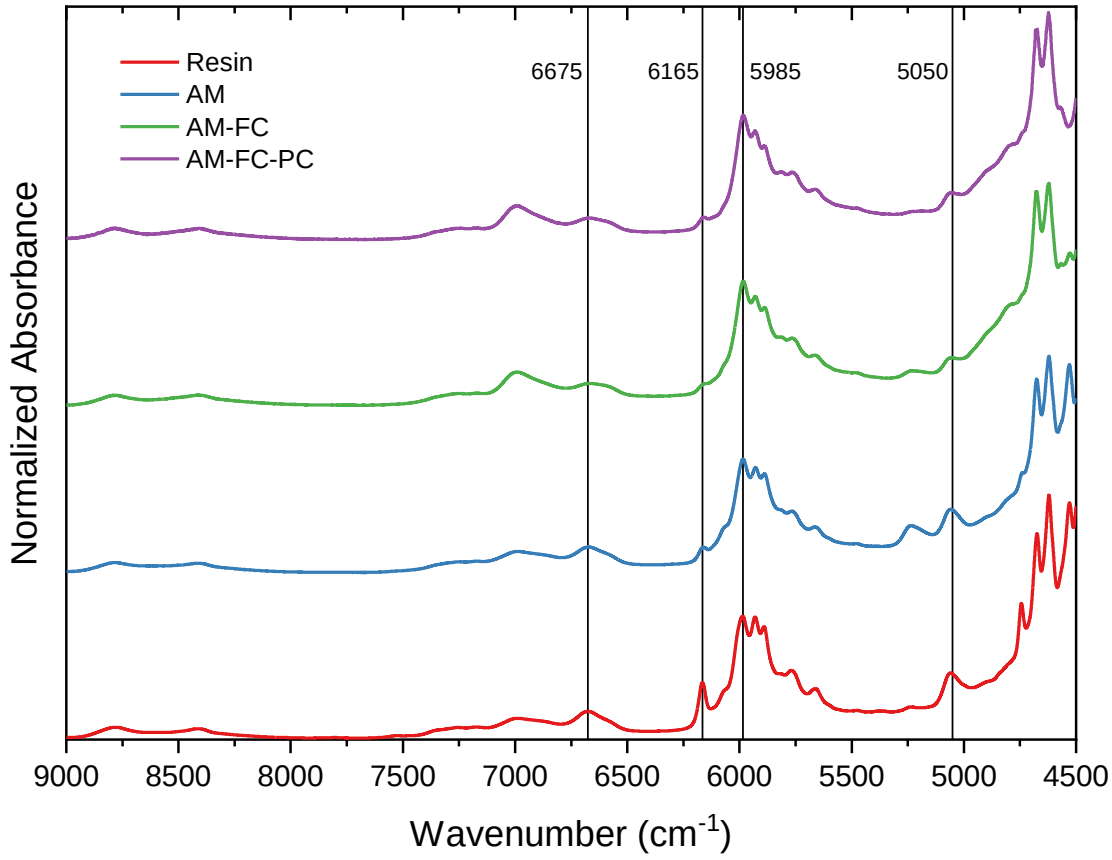

The extent of cure of both the methacrylate and amine networks are plotted in Figure 13, and the corresponding values are tabulated in Table 3. Error bars in Figure 13 are small and represent one standard deviation from the mean. Generally, the methacrylate network achieves a final extent of cure of about 85-95% after postcuring, and the epoxy-amine network reaches 65-75%. Where the initial methacrylate extent of cure is higher, the final amine extent of cure tends to be lower. This trend is likely due to lower mobility of epoxy and amine species in the partially cured methacrylate network as

the initial methacrylate network has vitrified before the thermal post-curing steps. It is also evident that, in the matrix-only specimens, there are no clear trends in conversion as a function of layer height, particularly when only considering the final conversion after the PC step. This is an interesting result, as we expect some differences due to the layer-by-layer nature of additive manufacturing. This may be due to the non-linear range of cure times chosen (i.e. the cure time for 200 μm layer height is not twice that of 100 μm layer height). Any trends may emerge if each cure time was a multiple of the layer height. However, the lack of an apparent trend does suggest that the layer height has little influence on the final conversion, and that, for composites, an appropriate layer height may be chosen based on the fiber mat thickness only and conversion differences do not need to be considered. Additionally, there is little difference between the two different orientations printed at 200 μm layer height. It is of note that the flat-printed sample had a lower methacrylate extent of cure after the AM step, but ultimately a higher final methacrylate conversion. The opposite trend exists in the amine conversion, which is likely due to molecular mobility in the network as described before.

Figure 13

Conversion as a Function of Printing Stage for a) 100 µm Edge, b) 200 µm Edge, c) 300 µm Edge, and d) 200 µm Flat Matrix Samples

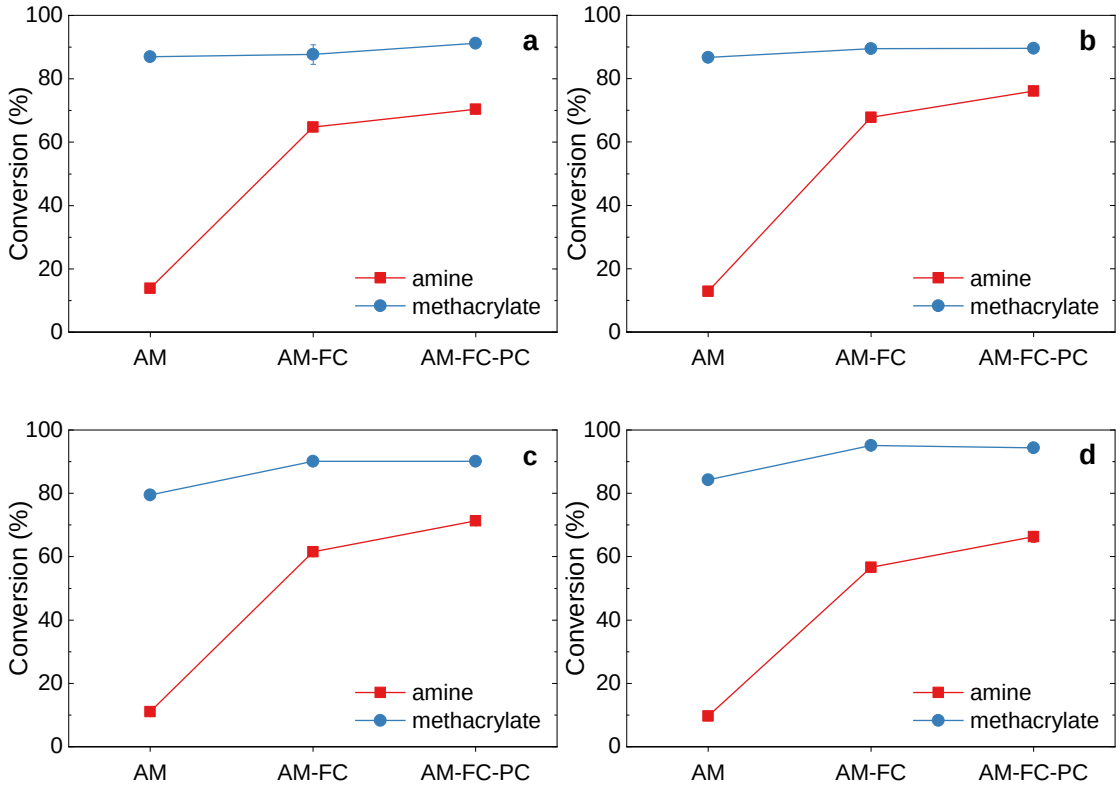

Table 3

Summarized Extent of Cure Values

	Curing Stage	$\alpha_{methacrylate}$ **(%)**	α_{amine} **(%)**
100 μm, edge	AM	86.89 ± 0.76	-
	AM-FC	87.68 ± 3.07	64.77 ± 1.06
	AM-FC-PC	91.16 ± 0.69	70.33 ± 0.78
200 μm, edge	AM	87.62 ± 1.26	-
	AM-FC	90.58 ± 0.83	67.84 ± 0.34
	AM-FC-PC	90.55 ± 0.21	76.04 ± 0.45
300 μm, edge	AM	81.34 ± 0.72	-
	AM-FC	91.39 ± 0.50	61.57 ± 0.33
	AM-FC-PC	91.53 ± 0.17	71.35 ± 1.03
200 μm, flat	AM	84.23 ± 0.03	-
	AM-FC	95.08 ± 0.88	56.61 ± 0.89
	AM-FC-PC	94.46 ± 0.54	66.27 ± 1.71
25% FL, flat	AM	79.15 ± 0.40	-
	AM-FC	92.85 ± 0.33	61.32 ± 0.33
	AM-FC-PC	91.71 ± 1.69	67.73 ± 0.22
25% FL, edge, 70 s	AM	80.44 ± 3.38	-
	AM-FC	89.0 ± 1.55	67.17 ± 0.37
	AM-FC-PC	82.71 ± 0.08	76.54 ± 0.15
25% FL, edge, 90 s	AM	83.32 ± 0.79	-
	AM-FC	91.42 ± 3.29	62.33 ± 0.89
	AM-FC-PC	90.01 ± 2.74	66.31 ± 5.43

For the composites, several trends are evident. First, the initial methacrylate extent of cure is generally lower than that of the matrix-only samples. It is likely that the fiber mats block some of the light from penetrating through to the matrix, and either the fibers themselves or the sizing surface treatment absorbs some light. Even though the fibers are transparent in the visible region, the fibers or the sizing may absorb in the UV, which comprises some of the projector output. This means that less light is available for initiating cleavage in the photoinitiator, and the lower concentration of photoinitiator radicals ultimately results in less conversion in the AM step. Also, generally, samples that have a lower initial methacrylate cure exhibit a higher final amine extent of cure. This effect is again attributed to lower epoxy or amine molecular mobility as a result of a more densely crosslinked methacrylate network.

4.3.3 Thermomechanical Properties

In order to determine the effect of layer height and orientation on the matrix and composites, DMA thermograms were collected as described in Chapter 3 for all samples fabricated. Exemplar thermograms for all matrix samples are shown in Figure 14. Storage modulus at 25 °C, peak of the loss modulus, and peak of the tan δ curves are tabulated in Table 4. Overall, there are few differences between matrix samples as a function of layer height. There is a slight β-transition evident as a shoulder on the loss modulus curve around 25 °C, which vary in size slightly depending on the layer height. The glass transition temperature, determined from the peak of the tan δ curve, is 115.7 ± 2.1 °C averaged over all the matrix samples. This is lower than what has been reported for PM-EM828 in the literature, but the different printing technique and slightly lower

methacrylate conversion may account for this difference [90]. While it is expected that varying layer height will have an effect on properties on the micro- or nanoscale, these results suggest that layer height has no impact on the macroscale thermomechanical properties.

Figure 14

DMA Thermograms for a) 100 µm Edge, b) 200 µm Edge, c) 300 µm Edge, and d) 200 µm Flat Matrix Samples

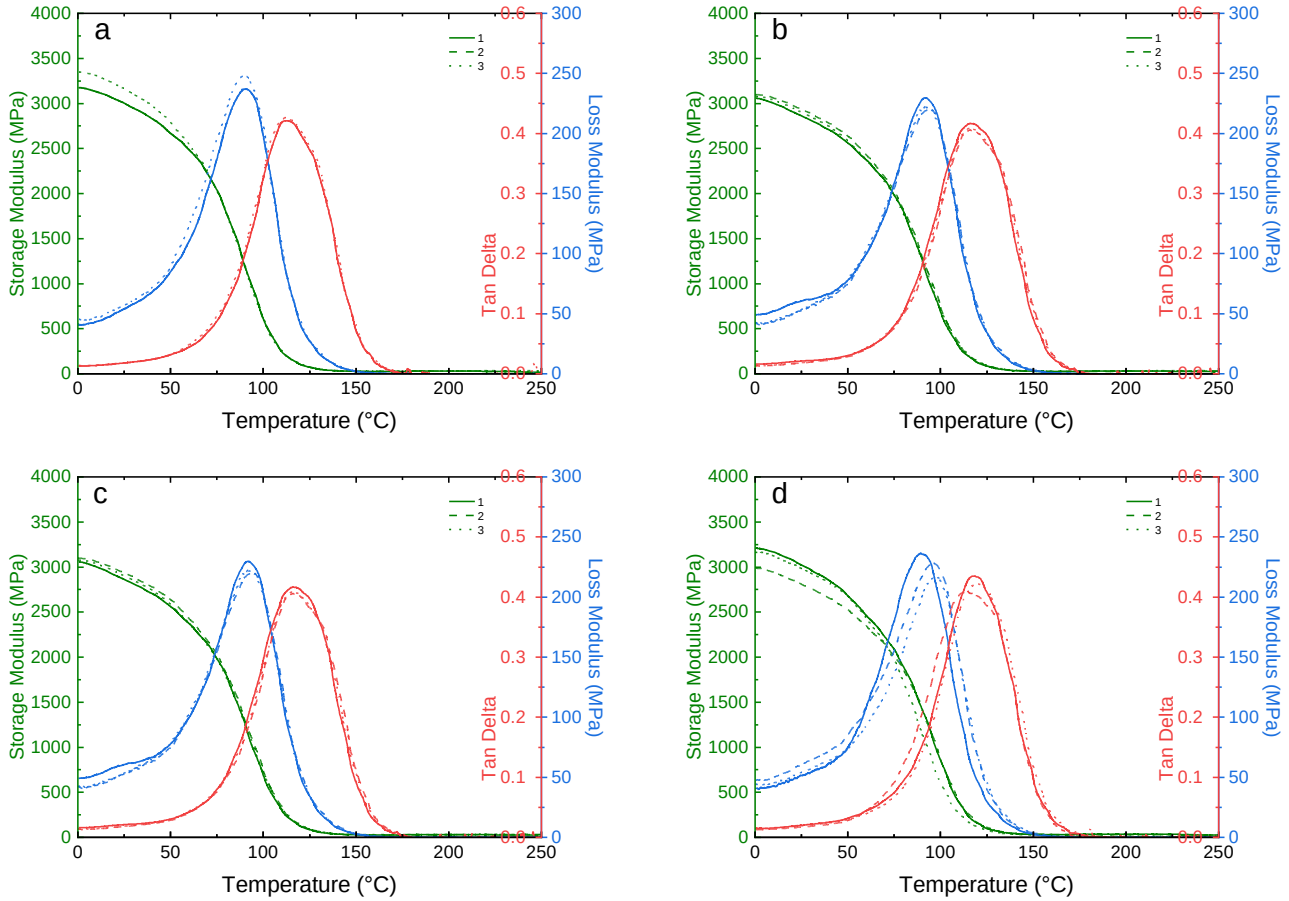

Table 4

Summarized DMA Data for Matrix and Composites

Sample Name	E'@ 25 °C (GPa)	Peak of E'' (°C)	Peak of tan δ (°C)
100 μm, edge	2.92 ± 0.27	91.2 ± 2.7	114.0 ± 3.5
200 μm, edge	2.90 ± 0.05	92.4 ± 0.7	116.3 ± 0.8
300 μm, edge	2.92 ± 0.15	96.7 ± 1.8	118.5 ± 0.7
200 μm, flat	2.85 ± 0.07	89.3 ± 0.5	114.2 ± 4.3
25% FL, flat	3.72 ± 0.20	97.1 ± 2.1	112.8 ± 0.01
25% FL edge, 70s	3.61 ± 0.32	81.6 ± 0.8	99.1 ± 0.3
25% FL edge, 90s	2.90 ± 0.39	94.5 ± 0.8	106.1 ± 1.28

All composites produced were tested in the same way as the matrix. DMA thermograms of all composites tested are shown in Figure 15. Of note was fiber-matrix debonding after the DMA test for the edge-printed samples. This is likely the reason for the low (on par with the matrix alone) glassy storage modulus in the 200 μm w/ 25% FL, edge, 90s samples. Representative samples after the DMA test are shown in Figure 16a-b. The fiber-matrix debonding evident in the edge-printed samples is likely due to the very small contact area between the fiber mats and the matrix. This may also be due to mismatched thermal expansion during the test, as the DMA tests were run well past the glass transition temperature into the rubbery plateau. A single Poisson's ratio (0.35) was used for all DMA tests run; this value was chosen because it is typically sufficient for rigid thermosetting materials [108, 115]. However, introduction of fiber reinforcing

material does change the Poisson's ratio, and a review of the literature indicates that woven glass fiber and epoxy composites have widely varying Poisson's ratios depending on orientation, fiber loading, and fiber identity [115-118]. Further work in this area is needed to understand how fiber inclusions impact the Poisson's ratio.

Figure 15

DMA Thermograms for a) 25% FL Edge 70 s, b) 25% FL Edge 90 s, and c) 25% FL Flat

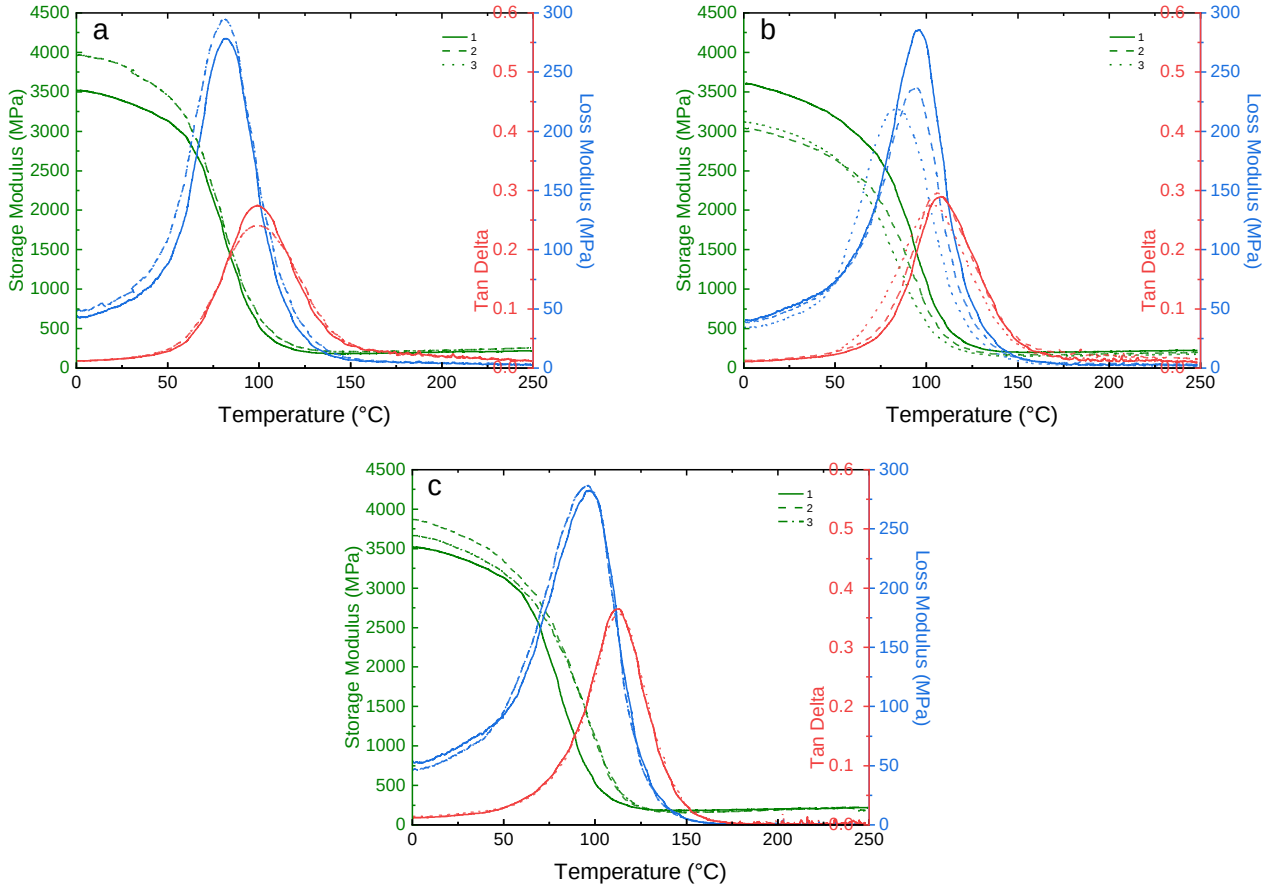

Figure 16

Evidence of Fiber-Matrix Debonding in an Edge-Printed Sample

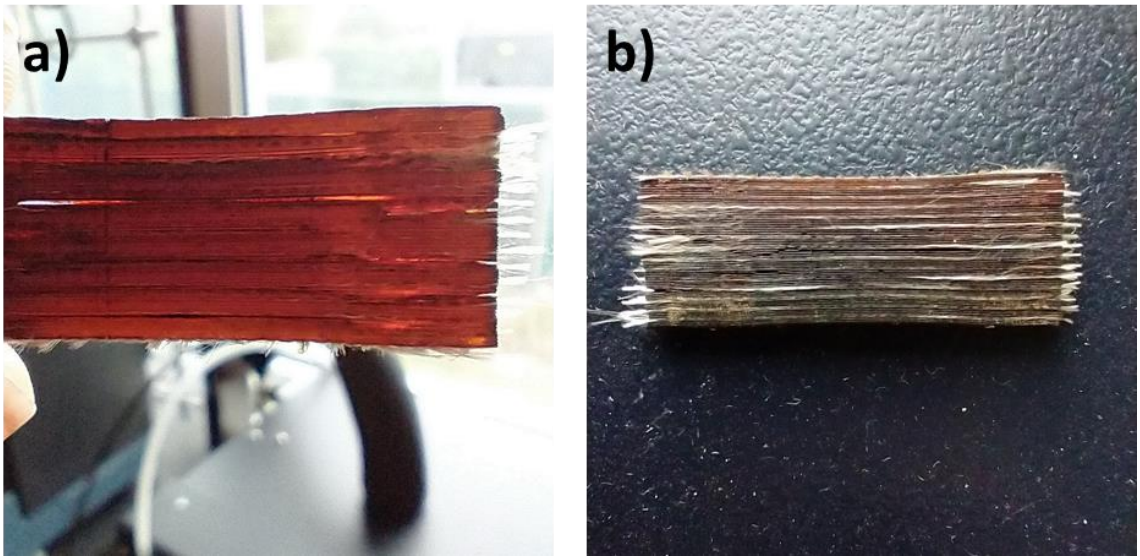

The composites exhibit several trends both relative to each other and relative to the neat matrix. Generally, the edge-printed composites show a clear drop in T_g and a small drop in the peak of E'' compared to the neat matrix for all samples tested. A similar drop in T_g relative to the neat matrix has been demonstrated before in epoxy-fiberglass composites [115]. The height of the tan δ peak is also a measure of damping ability; all composites show a lower height of the tan δ (ca. 0.4 in matrix vs. 0.3 in composites). This trend is expected, as the composites are generally expected to be stiffer and therefore less able to dissipate energy. Both the edge-printed composite samples and flat composite samples exhibit a boost in glassy storage modulus, relative to the matrix, at room temperature. The highest performance was achieved by the flat-printed sample for all metrics evaluated. This is due to the orientation; as discussed before, there was fiber-matrix debonding evident in all edge-printed composites after the test, and none was

visible for flat-printed samples. The loss of stiffness because of the debonding is likely why the T_g values are lower for edge-printed samples but approaching that of the matrix for flat-printed samples. The flat-printed composite achieved the highest peak of the loss modulus of any samples tested which suggests that the reinforcing fibers help the polymer maintain some stiffness, even as it goes through the glass transition. It is therefore critically important to consider part orientation to maximize surface contact between the matrix and fiber mats when printing fiber-reinforced composites.

Chapter 5

Conclusions and Future Work

5.1 Conclusions

The goal of this work was to produce a fully automated digital light projection VPP printer that places fiber reinforcements in-situ and evaluate the printability of fiberglass-reinforced composites in general. Two design iterations of the printer were produced, and the most recent version was designed for a commercial, woven fiberglass material. A basic test of this system has been carried out, and the fiber handling, optical/display, and resin vat/build platform systems have been shown to function as expected.

The feasibility of printing composites on this printer was also demonstrated by hand-placing mats and otherwise using the printer as designed. It was found that the same exposure time could be used for both the matrix and composites, suggesting that the light source is not attenuated by the particular fiber mats used. This is a potential advantage over laser-based stereolithography or other monochromatic printing techniques, where sizing on the fibers or the fibers themselves may absorb at the emission wavelength. This may happen in the custom printer as well, since there is a broad range of emission wavelengths, and it is likely that there is some overlap of absorption from either the fibers or sizing. However, the broad-spectrum light utilized in the custom printer is more flexible than a monochromatic light, since any small absorption by the fiber reinforcements is unlikely to span the entire emission range of the bulb, and there is sufficient light remaining to initiate the free-radical polymerization reaction. It was also demonstrated that a relatively high-viscosity resin for a printer without a resin deposition

system (1172 cP at 25 °C) [90] is printable on the custom printer. Furthermore, the viscosity was sufficiently low that good fiber wet-out and minimal voids were achieved. In flat-printed composites, the adhesion between the fibers and resin system were sufficient to withstand a DMA test without debonding.

The matrix and composites printed on the custom printer showed relatively good agreement with the thermomechanical properties reported in the literature [90]. The T_g was found to be approx. 115 °C for the matrix itself, which is lower than that reported in the literature by about 23 °C. The peak of the loss modulus is also slightly lower than what has been previously reported (approx. 90-95 °C vs 103 °C). Further work is needed to determine if these two differences are a function of the different printing method (DLP vs. SLA) or some other factor. It is possible that the lower AM step methacrylate conversion achieved in the DLP printer causes a slightly different network to be formed; as has been demonstrated, lower initial methacrylate conversion leads to higher amine conversion in the fully postcured part. It is therefore possible that the network formed by the two printing methods is different and would exhibit different thermal properties. However, the glassy storage modulus (E' at 25 °C) of 2.9 GPa does not show a statistically significant difference than what has been previously reported (3.1 GPa). Any network differences between the two printing methods evidently only impact the glass transition into the rubbery region, and do not have a substantial impact on glassy properties.

5.2 Future Work

5.2.1 Custom Printer

This work has produced a functional printer prototype. However, there is plenty of room for improvement to the design. To further improve on the printer itself, several changes are recommended that would greatly improve the utility and ease of use of the printer. First, the addition of an on-board laser cutter is suggested. This laser cutter could use the same sliced images as the projector in order to cut out the cross-section for each layer. This would result in less trimming needed on the finished part, as well as more efficient use of fiber tapes. In the current design, the square cut-outs must have a large distance between them, so that the tape is structurally able to withstand being pulled through the system. If cut-outs are placed too close together, the tape is prone to buckling, stretching, and warping. A laser cutter would allow for cutting just before the mat must be lowered into the vat, and the tape would maintain its strength in the velocity motor region. In conjunction with the laser cutter, an optical sensor would be advantageous to aid in precise placement of the cut-outs. Currently, the design is reliant on accurate dispensing from the velocity motor. While stepper motors are quite accurate, there is no accommodation for variations in the tape, such as uneven tension in the wound tape or fiber stretching. Over the course of a print, any variation due to uneven tension would be propagated through, and it is possible that alignment would deviate unacceptably from the original placement. An optical sensor in conjunction with appropriate placement of markers in the tape would ensure accurate positioning.

Another practical adjustment is to replace the build platform with a larger plate so that more parts can be printed at once. The existing build platform was designed to fit

with the smaller fiber frames in Prototype 1, but the current design does not use these frames and therefore the width and length are not as tightly constrained. A larger build platform would also provide flexibility in the size and orientation of parts printed. As described in Chapter 4, the orientation of the part relative to the fiber tape is critically important to maintain dimensional accuracy and limit fiber-matrix debonding. A larger platform would allow the user more space to orient the parts appropriately.

Finally, using a custom-built graphical user interface and slicer program would provide more flexibility in the control of the printer and make it more adaptable to a research environment. Currently, the printer cannot take gcode generated in another program and run it. This prevents users from writing their own gcode, and means that they are limited to the tools in the nanoDLP program. Normal usage of Prototype 2 does not require custom gcode. However, if the laser cutter system were implemented, it is unlikely that nanoDLP can handle the controls for this system. A custom system would therefore be needed to generate the toolpaths and add synchronized laser control. This system could be either a custom-written program from scratch or a modified version of nanoDLP. NanoDLP does allow for modifications to the source code, and so the interface could be customized without the need to start from scratch. Recommended modifications include adding an emergency stop button to interrupt any commands on the stack and stop all motion immediately. The built-in stop code is executed in the stack, and so any commands that have been previously sent must be completed before the stop command. Furthermore, a control panel that allows all tools to be jogged (moved in small increments) would significantly streamline the testing process and make the printer more user-friendly. Jog commands, or any other gcode commands, are executable via writing

and sending the appropriate code in the gcode terminal. However, this is not user-friendly for users who do not have coding experience and is unwieldy in a design and testing environment.

5.2.2 Printing and Characterizing Composites

The work described in Chapters 3 and 4 serves as a proof-of-concept for printing composites on the custom printer. There is plenty to explore further in the fabrication method, fiber feedstocks, and characterization methods. It was shown that fiber-matrix adhesion was sufficiently high to withstand a DMA test in flat-printed samples.

A full test print utilizing the custom printer is suggested in tandem with a set of 100% FL prints (fibers placed in every layer) fabricated by hand-placing the mats. This would provide a direct comparison between fiber placement methods. It is likely that there will be increased void fraction evident in automated composites since there is no ability to smooth out the mats by hand. However, the samples fabricated with automated fiber placement are likely to have better and more consistent fiber alignment. The mats are kept under high tension in the automated tape system, so the mats have little room to shift or otherwise be misaligned. In this study, layer height could be varied to determine the effect of high fiber loading on the resulting properties. In particular, testing both layer heights approximately equal to the fiber mat thickness and layer heights much more than the fiber mat thickness would provide insight on the effect of resin-rich regions within the printed part. Resin-rich regions have been shown previously to have a significant effect on interlaminar toughness [74]. While Prototype 2 is designed to place mats on every layer, resin-rich regions are possible by varying the layer height.

It is recommended to fabricate composites utilizing one or more other resin systems to determine if there is an effect of resin viscosity or chemistry on the resulting properties. The sequential IPN resin in this study may exhibit better interlayer adhesion than single-cure resins due to its sequential nature. While the methacrylate conversion likely forms a gradient through the part due to the AM process, the epoxy-amine system is expected to be homogenous throughout the part, since it is cured all at once. It is expected that this would promote interlayer bonding. Similarly, it is recommended that several fiber feedstocks be tested. Of particular interest for this project are PEKK or carbon fiber reinforcements due to their very high thermal properties and, in the case of carbon fiber, lightweighting potential. These fiber feedstocks may introduce difficulties curing the resin on the top side of the mats if the areal density is too high, or the material is not optically transparent enough. This would result in a steep conversion profile across a layer or, in the extreme case, no curing at all on the top side. Insufficient curing may preclude these fiber feedstocks from being used in this technique. However, a steep conversion profile may be acceptable, if the conversion is high enough that the part can hold its shape through postcuring. Addition of a high-temperature (well above room temperature) free-radical thermal initiator to the resin formulation may further mitigate these concerns.

Additional characterization of the fabricated composites is necessary to understand the mechanical properties as well as the failure mechanisms. Tensile testing is recommended as an initial screening. Tensile testing uses a similar amount of material as DMA when ASTM D638 Type V specimens are used, so it is appropriate as a screening technique [119]. If the larger build platform suggested in this section is implemented,

Type IV specimens could also be used. Tensile strength, Young's modulus, and strain at break are recommended metrics. In conjunction with tensile testing, scanning electron microscopy (SEM) to visualize the fracture surface would be advantageous. SEM would provide insight on whether failure starts with fiber-matrix debonding, matrix failure, etc. Fiber pull-out or breakage should also be evaluated. Furthermore, the morphology of printed layers could be examined, and positioning of the fiber mat relative to the layer could be determined. Comparisons between fiber mats placed by hand and mats placed by the custom printer may guide further changes to the custom printer.

Beyond tensile testing, some advanced characterization techniques would yield further depth of understanding about material properties and performance. In this work, an overall conversion was determined for both methacrylate and amine functional groups. This was a bulk measurement; however, spatially resolved FTIR would provide additional insight regarding conversion within a layer. This would be of interest both for the matrix layer height study as well as for composites, especially on the top side of a fiber mat. This would be particularly relevant for non-transparent reinforcements like carbon fiber or PEKK as mentioned previously. This work could also confirm whether the epoxy-amine extent of cure is uniform throughout, as hypothesized, or if a gradient is apparent. A gradient in the epoxy-amine cure is possible because the two networks are covalently linked via EM828.

Finally, to understand mechanical properties at the nanoscale, atomic force microscopy (AFM) is suggested. AFM can measure both force and topology. If AFM is employed to examine a fractured surface, spatially resolved Young's modulus could be measured within a layer and around the fiber reinforcement. This would provide

additional insight into how the fiber mats interact with the resin, as well as how the dual-cure IPN resin may differ from single-cure resins. Recent work has explored mechanical properties of VPP parts at the nanoscale [60, 120, 121]; however, existing work has not made use of a dual-cure IPN resin system, and there may be mechanical property differences as a result of the dual cure.

References

[1] "History of Composites." American Composites Manufacturers Association. http://compositeslab.com/composites-101/history-of-composites/ (accessed July 26, 2021).

[2] R. R. Nagavally, "Composite materials-history, types, fabrication techniques, advantages, and applications," *Int J Mech Prod Eng*, vol. 5, no. 9, pp. 82-7, 2017.

[3] S. Mazumdar, D. Pichler, M. Benevento, W. Seneviratine, R. Liang, and E. Witten. (2020, January 3) 2020 State of the Industry Report. *Composites Manufacturing*. Available: http://compositesmanufacturingmagazine.com/2020/01/2020-state-of-the-industry-report/

[4] P. K. Mallick, *Fiber-reinforced composites: materials, manufacturing, and design*. CRC press, 2007.

[5] "Composites By The Numbers." https://acmanet.org/composites-industry-overview/ (accessed July 26, 2021).

[6] A. R. Bunsell, S. Joannès, and A. Thionnet, *Fundamentals of fibre reinforced composite materials*. CRC Press, 2021.

[7] M. Yakout and M. Elbestawi, "Additive manufacturing of composite materials: an overview," in *6th International Conference on Virtual Machining Process Technology (VMPT), Montréal, May 29th–June 2nd*, 2017.

[8] A. Taub, E. De Moor, A. Luo, D. K. Matlock, J. G. Speer, and U. Vaidya, "Materials for automotive lightweighting," *Annual Review of Materials Research*, vol. 49, pp. 327-359, 2019.

[9] J. Plocher and A. Panesar, "Review on design and structural optimisation in additive manufacturing: Towards next-generation lightweight structures," *Materials & Design*, vol. 183, p. 108164, 2019.

[10] R. N. Lane and N. Rappaport, "Notes from the Field: Interview with Greg Mark, Founder and CEO of Markforged," in *The Design of Urban Manufacturing*: Routledge, 2020, pp. 19-26.

[11] R. V. Morgan *et al.*, "Markforged Continuous Fiber Composite Material Testing," Los Alamos National Lab.(LANL), Los Alamos, NM (United States), 2020.

[12] Y. Sano, R. Matsuzaki, M. Ueda, A. Todoroki, and Y. Hirano, "3D printing of discontinuous and continuous fibre composites using stereolithography," *Additive Manufacturing,* vol. 24, pp. 521-527, 2018/12/01/ 2018, doi: https://doi.org/10.1016/j.addma.2018.10.033.

[13] R. Advincula, "Toughening 3D printed polymers and nanocomposites," (in English), *Abstr. Pap. Am. Chem. Soc.,* Meeting Abstract vol. 256, p. 1, Aug 2018. [Online]. Available: <Go to ISI>://WOS:000447609104210.

[14] J. R. C. Dizon, Q. Y. Chen, A. D. Valino, and R. C. Advincula, "Thermo-mechanical and swelling properties of three-dimensional-printed poly (ethylene glycol) diacrylate/silica nanocomposites," (in English), *Mrs Commun,* vol. 9, no. 1, pp. 209-217, Mar 2019, doi: 10.1557/mrc.2018.188.

[15] N. A. Nguyen, C. C. Bowland, and A. K. Naskar, "general method to improve 3D-printability and inter-layer adhesion in lignin-based composites," (in English), *Appl Mater Today,* vol. 12, pp. 138-152, Sep 2018, doi: 10.1016/j.apmt.2018.03.009.

[16] L. Haitao and M. Jianhua, "Study on Nanosilica Reinforced Stereolithography Resin," *Journal of Reinforced Plastics and Composites,* vol. 29, no. 6, pp. 909-920, 2009, doi: 10.1177/0731684409102838.

[17] G. Gonzalez *et al.*, "Development of 3D printable formulations containing CNT with enhanced electrical properties," *Polymer,* vol. 109, pp. 246-253, Jan 2017, doi: 10.1016/j.polymer.2016.12.051.

[18] C. Altinkok, T. Uyar, M. A. Tasdelen, and Y. Yagci, "In Situ Synthesis of Polymer/Clay Nanocomposites by Type II Photoinitiated Free Radical Polymerization," (in English), *J Polym Sci Pol Chem,* vol. 49, no. 16, pp. 3658-3663, Aug 15 2011, doi: 10.1002/pola.24788.

[19] X. Feng, Z. Yang, S. Chmely, Q. Wang, S. Wang, and Y. Xie, "Lignin-coated cellulose nanocrystal filled methacrylate composites prepared via 3D stereolithography printing: Mechanical reinforcement and thermal stabilization," *Carbohydr Polym,* vol. 169, pp. 272-281, Aug 1 2017, doi: 10.1016/j.carbpol.2017.04.001.

[20] Z. Weng, Y. Zhou, W. Lin, T. Senthil, and L. Wu, "Structure-property relationship of nano enhanced stereolithography resin for desktop SLA 3D printer," *Composites Part A: Applied Science and Manufacturing,* vol. 88, pp. 234-242, 2016, doi: 10.1016/j.compositesa.2016.05.035.

[21] G. Taormina, C. Sciancalepore, F. Bondioli, and M. Messori, "Special Resins for Stereolithography: In Situ Generation of Silver Nanoparticles," *Polymers,* vol. 10, no. 2, 2018, doi: 10.3390/polym10020212.

[22] M. R. Douglass, M. Hatzenbichler, M. Geppert, R. Seemann, J. Stampfl, and P. I. Oden, "Additive manufacturing of photopolymers using the Texas Instruments DLP lightcrafter," presented at the Emerging Digital Micromirror Device Based Systems and Applications V, 2013. [Online]. Available: https://www.spiedigitallibrary.org/conference-proceedings-of-spie/8618/86180A/Additive-manufacturing-of-photopolymers-using-the-Texas-Instruments-DLP-lightcrafter/10.1117/12.2001651.pdf.

[23] J. Z. Manapat, Q. Chen, P. Ye, and R. C. Advincula, "3D Printing of Polymer Nanocomposites via Stereolithography," *Macromolecular Materials and Engineering*, vol. 302, no. 9, 2017, doi: 10.1002/mame.201600553.

[24] M. R. Douglass *et al.*, "DLP-based light engines for additive manufacturing of ceramic parts," presented at the Emerging Digital Micromirror Device Based Systems and Applications IV, 2012. [Online]. Available: https://www.spiedigitallibrary.org/conference-proceedings-of-spie/8254/82540E/DLP-based-light-engines-for-additive-manufacturing-of-ceramic-parts/10.1117/12.907113.pdf.

[25] J. E. Sumerak and J. D. Martin, "Pultrusion process variables and their effect upon manufacturing capability," in *Composites go to market. SPI Annual conference preprint. 39*, 1984, pp. 1. B. 1-1. B. 7.

[26] I. R. Gibson, D.; Stucker, B., *Additive Manufacturing Technology*. Springer, Boston, MA, 2010.

[27] P. F. Jacobs, "Rapid prototyping & manufacturing— Fundamentals of stereolithography," vol. 12, ed: Elsevier Ltd, 1993, pp. 430-433.

[28] G. N. Levy, R. Schindel, and J. P. Kruth, "Rapid Manufacturing and Rapid Tooling With Layer Manufacturing (LM) Technologies, State of the Art and Future Perspectives," *CIRP Annals*, vol. 52, no. 2, pp. 589-609, 2003/01/01/ 2003, doi: https://doi.org/10.1016/S0007-8506(07)60206-6.

[29] S. H. Khajavi, J. Partanen, and J. Holmström, "Additive manufacturing in the spare parts supply chain," *Computers in Industry*, vol. 65, no. 1, pp. 50-63, 2014/01/01/ 2014, doi: https://doi.org/10.1016/j.compind.2013.07.008.

[30] "Print me a jet engine." The Economist. https://www.economist.com/schumpeter/2012/11/22/print-me-a-jet-engine (accessed October 2, 2019).

[31] G. Allevi, M. Cibeca, R. Fioretti, R. Marsili, R. Montanini, and G. Rossi, "Qualification of additively manufactured aerospace brackets: A comparison between thermoelastic stress analysis and theoretical results," *Measurement*, vol. 126, pp. 252-258, 2018/10/01/ 2018, doi: https://doi.org/10.1016/j.measurement.2018.05.068.

[32] R. Huang *et al.*, "Energy and emissions saving potential of additive manufacturing: the case of lightweight aircraft components," *Journal of Cleaner Production*, vol. 135, pp. 1559-1570, 2016/11/01/ 2016, doi: https://doi.org/10.1016/j.jclepro.2015.04.109.

[33] Y. Yang, L. Li, Y. Pan, and Z. Sun, "Energy consumption modeling of stereolithography-based additive manufacturing toward environmental sustainability," *Journal of Industrial Ecology*, vol. 21, no. S1, pp. S168-S178, 2017.

[34] M. Baumers, "Economic aspects of additive manufacturing: benefits, costs and energy consumption," © Martin Baumers, 2012.

[35] J. Watson and K. Taminger, "A decision-support model for selecting additive manufacturing versus subtractive manufacturing based on energy consumption," *Journal of Cleaner Production*, vol. 176, pp. 1316-1322, 2018.

[36] M. Baumers, C. Tuck, R. Wildman, I. Ashcroft, E. Rosamond, and R. Hague, "Transparency built-in: Energy consumption and cost estimation for additive manufacturing," *Journal of Industrial Ecology*, vol. 17, no. 3, pp. 418-431, 2013.

[37] W. K. P. O. B. Swainson, Berkeley, CA, 94704), "Method, medium and apparatus for producing three-dimensional figure product," United States Patent Appl. 4041476, 1977. [Online]. Available: http://www.freepatentsonline.com/4041476.html

[38] C. W. Hull, "Apparatus for production of three-dimensional objects by stereolithography," Patent US4575330A, 1986.

[39] N. Guo and M. C. Leu, "Additive manufacturing: technology, applications and research needs," *Frontiers of Mechanical Engineering*, journal article vol. 8, no. 3, pp. 215-243, September 01 2013, doi: 10.1007/s11465-013-0248-8.

[40] O. Fergani, F. Berto, T. Welo, and S. Y. Liang, "Analytical modelling of residual stress in additive manufacturing," (in English), *Fatigue Fract Eng M*, vol. 40, no. 6, pp. 971-978, Jun 2017, doi: 10.1111/ffe.12560.

[41] S. C. Ligon, R. Liska, J. Stampfl, M. Gurr, and R. Mulhaupt, "Polymers for 3D Printing and Customized Additive Manufacturing," *Chem Rev*, vol. 117, no. 15, pp. 10212-10290, Aug 9 2017, doi: 10.1021/acs.chemrev.7b00074.

[42] S. Miao *et al.*, "4D printing smart biomedical scaffolds with novel soybean oil epoxidized acrylate," *Sci Rep*, vol. 6, p. 27226, Jun 2 2016, doi: 10.1038/srep27226.

[43] M. V. Bertolo, R. C. Moraes, C. Pfeifer, V. E. Salgado, A. R. Correr, and L. F. Schneider, "Influence of Photoinitiator System on Physical-Chemical Properties of Experimental Self-Adhesive Composites," *Braz Dent J,* vol. 28, no. 1, pp. 35-39, Jan-Feb 2017, doi: 10.1590/0103-6440201700841.

[44] J. W. Stansbury and M. J. Idacavage, "3D printing with polymers: Challenges among expanding options and opportunities," *Dent Mater,* vol. 32, no. 1, pp. 54-64, Jan 2016, doi: 10.1016/j.dental.2015.09.018.

[45] H. Gong, M. Beauchamp, S. Perry, A. T. Woolley, and G. P. Nordin, "Optical Approach to Resin Formulation for 3D Printed Microfluidics," *RSC Adv,* vol. 5, no. 129, pp. 106621-106632, Dec 31 2015, doi: 10.1039/C5RA23855B.

[46] S. C. Ligon-Auer, M. Schwentenwein, C. Gorsche, J. Stampfl, and R. Liska, "Toughening of photo-curable polymer networks: a review," *Polymer Chemistry,* 10.1039/C5PY01631B vol. 7, no. 2, pp. 257-286, 2016, doi: 10.1039/C5PY01631B.

[47] S. Mansour, M. Gilbert, and R. Hague, "A study of the impact of short-term ageing on the mechanical properties of a stereolithography resin," *Materials Science and Engineering: A,* vol. 447, no. 1-2, pp. 277-284, 2007, doi: 10.1016/j.msea.2006.10.007.

[48] "Materials Data Sheet: Photopolymer Resin for Form 1+ and Form 2." https://archive-media.formlabs.com/upload/XL-DataSheet.pdf (accessed.

[49] "3D Systems On Demand- Stereolithography- Materials " https://www.3dsystems.com/on-demand-manufacturing/stereolithography-sla/materials (accessed.

[50] "A Material World: Our Materials." https://www.carbon3d.com/materials/ (accessed.

[51] M. Peerzada, S. Abbasi, K. T. Lau, and N. Hameed, "Additive Manufacturing of Epoxy Resins: Materials, Methods, and Latest Trends," *Industrial & Engineering Chemistry Research,* vol. 59, no. 14, pp. 6375-6390, 2020/04/08 2020, doi: 10.1021/acs.iecr.9b06870.

[52] J. V. Crivello, "A new visible light sensitive photoinitiator system for the cationic polymerization of epoxides," *Journal of Polymer Science Part A: Polymer Chemistry,* vol. 47, no. 3, pp. 866-875, 2009, doi: https://doi.org/10.1002/pola.23203.

[53] J. V. Crivello, "Radical-Promoted Visible Light Photoinitiated Cationic Polymerization of Epoxides," *Journal of Macromolecular Science, Part A,* vol. 46, no. 5, pp. 474-483, 2009/03/25 2009, doi: 10.1080/10601320902797707.

[54] S. Schüller-Ravoo, S. M. Teixeira, J. Feijen, D. W. Grijpma, and A. A. Poot, "Flexible and Elastic Scaffolds for Cartilage Tissue Engineering Prepared by Stereolithography Using Poly (trimethylene carbonate)-B ased Resins," *Macromolecular bioscience,* vol. 13, no. 12, pp. 1711-1719, 2013.

[55] C. Hinczewski, S. Corbel, and T. Chartier, "Ceramic suspensions suitable for stereolithography," *Journal of the European Ceramic Society,* vol. 18, no. 6, pp. 583-590, 1998.

[56] F. P. Melchels, J. Feijen, and D. W. Grijpma, "A poly (D, L-lactide) resin for the preparation of tissue engineering scaffolds by stereolithography," *Biomaterials,* vol. 30, no. 23-24, pp. 3801-3809, 2009.

[57] C. Hofstetter, S. Orman, S. Baudis, and J. Stampfl, "Combining cure depth and cure degree, a new way to fully characterize novel photopolymers," *Additive Manufacturing,* vol. 24, pp. 166-172, 2018/12/01/ 2018, doi: https://doi.org/10.1016/j.addma.2018.09.025.

[58] Y. Li, Q. Mao, J. Yin, Y. Wang, J. Fu, and Y. Huang, "Theoretical prediction and experimental validation of the digital light processing (DLP) working curve for photocurable materials," *Additive Manufacturing,* p. 101716, 2020.

[59] G. Arias-Ferreiro *et al.*, "Printability Study of a Conductive Polyaniline/Acrylic Formulation for 3D Printing," *Polymers,* vol. 13, no. 13, p. 2068, 2021.

[60] C. I. Higgins, T. E. Brown, and J. P. Killgore, "Digital light processing in a hybrid atomic force microscope: In Situ, nanoscale characterization of the printing process," *Additive Manufacturing,* vol. 38, p. 101744, 2021.

[61] Y. Li *et al.*, "High-fidelity and high-efficiency additive manufacturing using tunable pre-curing digital light processing," *Additive Manufacturing,* vol. 30, p. 100889, 2019.

[62] Y. Yang *et al.*, "Three dimensional printing of high dielectric capacitor using projection based stereolithography method," *Nano Energy,* vol. 22, pp. 414-421, 2016.

[63] R. Chen, Q. Lian, D. Li, X. He, S. Wang, and J. Zhuang, "Stereolithographic additive manufacturing diamond/SiC composites with high thermal conductivity for electronic 3D-packaging applications," *Ceramics International,* vol. 47, no. 10, pp. 14009-14020, 2021.

[64] H. Korhonen *et al.*, "Fabrication of graphene-based 3D structures by stereolithography," *physica status solidi (a),* vol. 213, no. 4, pp. 982-985, 2016.

[65] G. Scordo *et al.*, "A novel highly electrically conductive composite resin for stereolithography," *Materials Today Communications,* vol. 19, pp. 12-17, 2019.

[66] C. Sciancalepore, F. Moroni, M. Messori, and F. Bondioli, "Acrylate-based silver nanocomposite by simultaneous polymerization–reduction approach via 3D stereolithography," *Composites Communications,* vol. 6, pp. 11-16, 2017.

[67] S. A. Skoog, P. L. Goering, and R. J. Narayan, "Stereolithography in tissue engineering," *Journal of Materials Science: Materials in Medicine,* vol. 25, no. 3, pp. 845-856, 2014.

[68] F. P. Melchels, J. Feijen, and D. W. Grijpma, "A review on stereolithography and its applications in biomedical engineering," *Biomaterials,* vol. 31, no. 24, pp. 6121-6130, 2010.

[69] O. Guillaume *et al.*, "Surface-enrichment with hydroxyapatite nanoparticles in stereolithography-fabricated composite polymer scaffolds promotes bone repair," *Acta biomaterialia,* vol. 54, pp. 386-398, 2017.

[70] A. Ronca, L. Ambrosio, and D. W. Grijpma, "Preparation of designed poly (D, L-lactide)/nanosized hydroxyapatite composite structures by stereolithography," *Acta biomaterialia,* vol. 9, no. 4, pp. 5989-5996, 2013.

[71] F. M. Monticeli, R. M. Neves, H. L. Ornaghi Jr, and J. H. S. Almeida Jr, "A systematic review on high-performance fiber-reinforced 3D printed thermoset composites," *Polymer Composites*, 2021.

[72] J.-W. Choi, H.-C. Kim, and R. Wicker, "Multi-material stereolithography," *Journal of Materials Processing Technology,* vol. 211, no. 3, pp. 318-328, 2011.

[73] M. J. Holthaus, "Short Glass Fiber Reinforced Composites Manufactured by Stereolithography," North Dakota State University, 2021.

[74] M. Idrees, A. M. Ibrahim, E. Tekerek, A. Kontsos, G. R. Palmese, and N. J. Alvarez, "The effect of resin-rich layers on mechanical properties of 3D printed woven fiber-reinforced composites," *Composites Part A: Applied Science and Manufacturing,* vol. 144, p. 106339, 2021.

[75] N. Gupta and A. K. Srivastava, "Interpenetrating polymer networks: A review on synthesis and properties," *Polymer International*, vol. 35, no. 2, pp. 109-118, 1994, doi: https://doi.org/10.1002/pi.1994.210350201.

[76] J. R. Millar, "263. Interpenetrating polymer networks. Styrene–divinylbenzene copolymers with two and three interpenetrating networks, and their sulphonates," *Journal of the Chemical Society (Resumed),* 10.1039/JR9600001311 no. 0, pp. 1311-1317, 1960, doi: 10.1039/JR9600001311.

[77] U. Farooq, J. Teuwen, and C. Dransfeld, "Toughening of Epoxy Systems with Interpenetrating Polymer Network (IPN): A Review," *Polymers*, vol. 12, no. 9, p. 1908, 2020. [Online]. Available: https://www.mdpi.com/2073-4360/12/9/1908.

[78] B. N. V. S. Ganesh Gupta K, M. M. Hiremath, B. C. Ray, and R. K. Prusty, "Improved mechanical responses of GFRP composites with epoxy-vinyl ester interpenetrating polymer network," *Polymer Testing,* vol. 93, p. 107008, 2021/01/01/ 2021, doi: https://doi.org/10.1016/j.polymertesting.2020.107008.

[79] K. Okawa and S. Saito, "Resin composition for optical molding," Japan Patent JPH0275618A, 1988.

[80] S. Saito and K. Okawa, "Resin composition for optical modeling," Patent EP0360869A1, 1989.

[81] B. Steinmann, J.-P. Wolf, A. Schulthess, and M. Hunziker, "Photosensitive compositions," USA Patent US5476748A, 1993.

[82] J. Poelma, "1k alcohol dual cure resins for additive manufacturing," USA Patent US20200070409A1, 2019.

[83] M. S. Menyo and J. P. Rolland, "Cyanate ester epoxy dual cure resins for additive manufacturing," Patent US20200023576A1, 2019.

[84] M. S. Menyo, "Tough, high temperature polymers produced by stereolithography," USA Patent US20200070407A1, 2018.

[85] J. P. Rolland, "Dual cure resins containing microwave absorbing materials and methods of using the same," USA Patent US10500786B2, 2017.

[86] M. S. Menyo and L. M. Robeson, "Dual Cure Stereolithography Resins Containing Diels-Alder Adducts," USA Patent US20190322785A1, 2018.

[87] J. D. Drazba and J. P. Rolland, "Silicone Dual Cure Resins for Additive Manufacturing," USA Patent US20180244854A1, 2016.

[88] X. Gu and J. P. Rolland, "Cyclic ester dual cure resins for additive manufacturing," Patent US20170174827A1, 2016.

[89] J. P. Rolland *et al.*, "Polyurethane resins having multiple mechanisms of hardening for use in producing three-dimensional objects," USA Patent US9453142B2, 2016.

[90] A. W. Bassett, A. E. Honnig, J. J. La Scala, and J. F. Stanzione, "Network toughening of additively manufactured, high glass transition temperature materials via sequentially cured, interpenetrating polymers," *Polymer international,* 2020, doi: 10.1002/pi.6091.

[91] O. Konuray, A. Altet, J. Bonada, A. Tercjak, X. Fernández-Francos, and X. Ramis, "Epoxy Doped, Nano-scale Phase-separated Poly-Acrylates with Potential in 3D Printing," *Macromolecular Materials and Engineering,* vol. 306, no. 3, p. 2000558, 2021.

[92] T. Zhao *et al.*, "A comparative study on 3D printed silicone-epoxy/acrylate hybrid polymers via pure photopolymerization and dual-curing mechanisms," *Journal of Materials Science,* vol. 54, no. 6, pp. 5101-5111, 2019.

[93] Y. Cui, J. Yang, D. Lei, and J. Su, "3D printing of a dual-curing resin with cationic curable vegetable oil," *Industrial & Engineering Chemistry Research,* vol. 59, no. 25, pp. 11381-11388, 2020.

[94] R. Yu *et al.*, "Three-Dimensional Printing of Shape Memory Composites with Epoxy-Acrylate Hybrid Photopolymer," *ACS Applied Materials & Interfaces,* vol. 9, no. 2, pp. 1820-1829, 2017/01/18 2017, doi: 10.1021/acsami.6b13531.

[95] J. P. Fouassier and J. Lalevée, "Photochemical Production of Interpenetrating Polymer Networks; Simultaneous Initiation of Radical and Cationic Polymerization Reactions," *Polymers,* vol. 6, no. 10, pp. 2588-2610, 2014. [Online]. Available: https://www.mdpi.com/2073-4360/6/10/2588.

[96] Y.-J. Park, D.-H. Lim, H.-J. Kim, D.-S. Park, and I.-K. Sung, "UV- and thermal-curing behaviors of dual-curable adhesives based on epoxy acrylate oligomers," *International Journal of Adhesion and Adhesives,* vol. 29, no. 7, pp. 710-717, 2009/10/01/ 2009, doi: https://doi.org/10.1016/j.ijadhadh.2009.02.001.

[97] B. Martin, J. Puentes, L. Wruck, and T. A. Osswald, "Degree of cure of epoxy/acrylic photopolymers: Characterization with raman spectroscopy and a modified phenomenological model," *Polymer Engineering & Science,* vol. 58, no. 2, pp. 228-237, 2018, doi: 10.1002/pen.24550.

[98] T. Zhao, R. Yu, W. Huang, W. Zhao, and G. Wang, "Aliphatic silicone-epoxy based hybrid photopolymers applied in stereolithography 3D printing," *Polymers for Advanced Technologies,* vol. 32, no. 3, pp. 980-987, 2021.

[99] Z.-X. Zhou *et al.*, "High-Performance Cyanate Ester Resins with Interpenetration Networks for 3D Printing," *ACS applied materials & interfaces,* vol. 12, no. 34, pp. 38682-38689, 2020.

[100] H. Q. Yan, H. Q. Wang, and J. Cheng, "Interpenetrating polymer networks from the novel bismaleimide and cyanate containing naphthalene: Cure and thermal characteristics," (in English), *Eur Polym J,* vol. 45, no. 8, pp. 2383-2390, Aug 2009, doi: 10.1016/j.eurpolymj.2009.04.031.

[101] O. Konuray, X. Fernández-Francos, X. Ramis, and À. Serra, "State of the art in dual-curing acrylate systems," *Polymers,* vol. 10, no. 2, p. 178, 2018.

[102] D. A. Brennan, K. Shirvani, C. D. Rhoads, S. E. Lofland, and V. Z. Beachley, "Electrospinning and post-drawn processing effects on the molecular organization and mechanical properties of polyacrylonitrile (PAN) nanofibers," (in English), *Mrs Commun,* vol. 9, no. 2, pp. 764-772, Jun 2019, doi: 10.1557/mrc.2019.67.

[103] A. A. Conte *et al.*, "Effects of post-draw processing on the structure and functional properties of electrospun PVDF-HFP nanofibers," (in English), *Polymer,* vol. 171, pp. 192-200, May 8 2019, doi: 10.1016/j.polymer.2019.03.017.

[104] D. Jao and V. Z. Beachley, "Continuous Dual-Track Fabrication of Polymer Micro-/Nanofibers Based on Direct Drawing," (in English), *ACS Macro Letters,* vol. 8, no. 5, pp. 588-595, May 2019, doi: 10.1021/acsmacrolett.9b00167.

[105] D. A. Skoog, F. J. Holler, and S. R. Crouch, *Principles of instrumental analysis*. Cengage learning, 2017.

[106] M. G. González, J. C. Cabanelas, and J. Baselga, "Applications of FTIR on epoxy resins-identification, monitoring the curing process, phase separation and water uptake," *Infrared Spectroscopy-Materials Science, Engineering and Technology,* vol. 2, pp. 261-284, 2012.

[107] G. Socrates, *Infrared and Raman characteristic group frequencies: tables and charts*. John Wiley & Sons, 2004.

[108] K. P. Menard, *Dynamic mechanical analysis : a practical introduction*. Boca Raton, Fla: CRC Press, 1999.

[109] I. M. McAninch, G. R. Palmese, J. L. Lenhart, and J. J. La Scala, "DMA testing of epoxy resins: The importance of dimensions," *Polymer Engineering & Science,* vol. 55, no. 12, pp. 2761-2774, 2015, doi: 10.1002/pen.24167.

[110] J. F. Stanzione III, J. M. Sadler, J. J. La Scala, K. H. Reno, and R. P. Wool, "Vanillin-based resin for use in composite applications," *Green Chemistry,* vol. 14, no. 8, 2012, doi: 10.1039/c2gc35672d.

[111] W. Obande, D. Mamalis, D. Ray, L. Yang, and C. M. Ó Brádaigh, "Mechanical and thermomechanical characterisation of vacuum-infused thermoplastic- and thermoset-based composites," *Materials & Design,* vol. 175, p. 107828, 2019/08/05/ 2019, doi: https://doi.org/10.1016/j.matdes.2019.107828.

[112] S. Y. Nayak *et al.*, "Influence of fabric orientation and compression factor on the mechanical properties of 3D E-glass reinforced epoxy composites," *Journal of Materials Research and Technology,* vol. 9, no. 4, pp. 8517-8527, 2020/07/01/ 2020, doi: https://doi.org/10.1016/j.jmrt.2020.05.111.

[113] V. Sharma, M. L. Meena, M. Kumar, and A. Patnaik, "Waste Fly Ash Powder Filled Glass Fiber Reinforced Epoxy Composite: Physical, Mechancial, Thermo-mechanical, and Three-body Abrasive Wear Analysis," *Fibers and Polymers,* vol. 22, no. 4, pp. 1120-1136, 2021.

[114] M. Sheinbaum, L. Sheinbaum, O. Weizman, H. Dodiuk, and S. Kenig, "Toughening and enhancing mechanical and thermal properties of adhesives and glass-fiber reinforced epoxy composites by brominated epoxy," *Composites Part B: Engineering,* vol. 165, pp. 604-612, 2019.

[115] P. Ghosh, N. R. Bose, B. Mitra, and S. Das, "Dynamic mechanical analysis of FRP composites based on different fiber reinforcements and epoxy resin as the matrix material," *Journal of Applied Polymer Science,* vol. 64, no. 12, pp. 2467-2472, 1997.

[116] G. Zhou *et al.*, "Effects of fabric architectures on mechanical and damage behaviors in carbon/epoxy woven composites under multiaxial stress states," *Polymer Testing,* vol. 90, p. 106657, 2020.

[117] J. Ye, Y. Wang, Y. Wang, B. Shi, Y. Li, and X. Qiao, "Microscopic modeling and effective properties evaluation of glass/epoxy plain woven composites," *Materials Research Express,* vol. 5, no. 10, p. 105303, 2018.

[118] O. I. Okoli and G. F. Smith, "The effect of strain rate and fibre content on the Poisson's ratio of glass/epoxy composites," *Composite Structures,* vol. 48, no. 1, pp. 157-161, 2000/01/01/ 2000, doi: https://doi.org/10.1016/S0263-8223(99)00089-6.

[119] *Standard Test Method for Tensile Properties of Plastics,* D638-14, ASTM, West Conshohocken, PA, 2014.

[120] C. Ligget, "Materials Characterization of Short Carbon Fiber Reinforced Composite Fabricated via 3D Stereolithography," 2021.

[121] W. Li, M. B. Noodeh, N. Delpouve, J. Saiter, L. Tan, and M. Negahban, "Printing continuously graded interpenetrating polymer networks of acrylate/epoxy by manipulating cationic network formation during stereolithography," *Express Polymer Letters,* vol. 10, no. 12, p. 1003, 2016.

Appendix A

FTIR Spectra

Figure A1

Exemplar FTIR Spectra for 100 µm Edge Matrix Samples

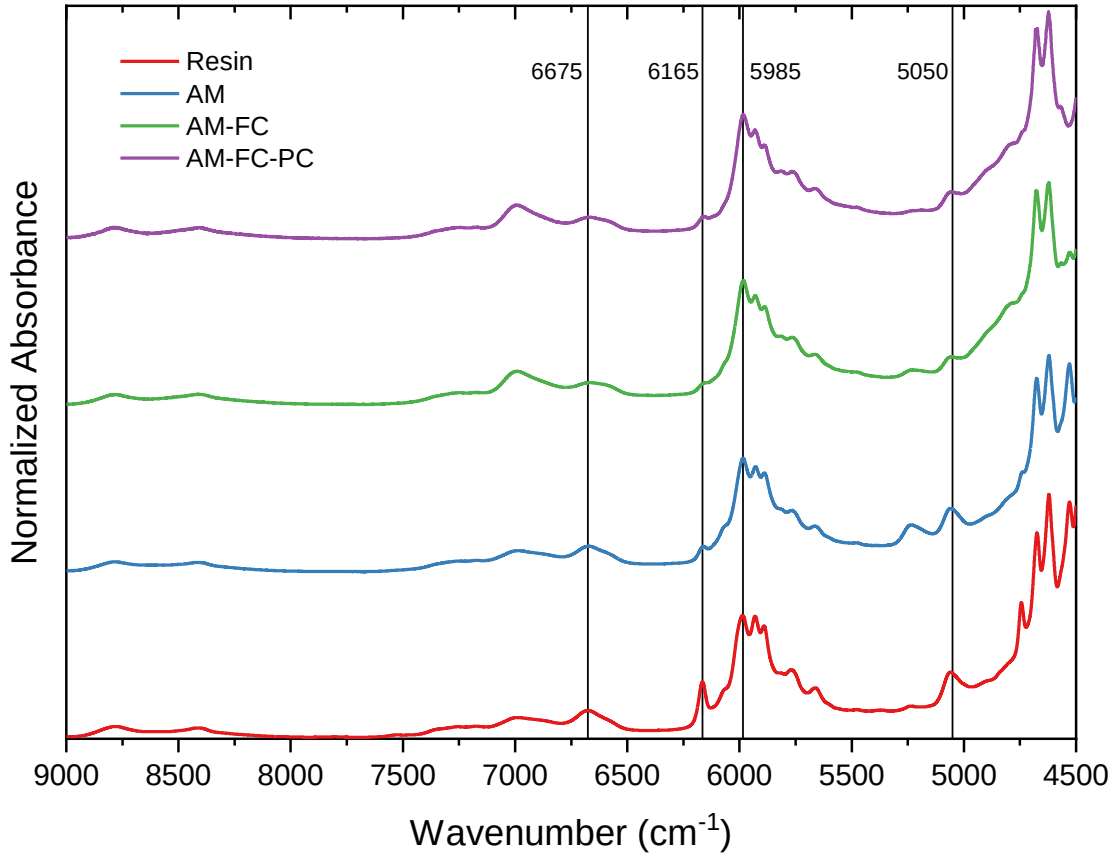

Figure A2

Exemplar FTIR Spectra for 200 µm Edge Matrix Samples

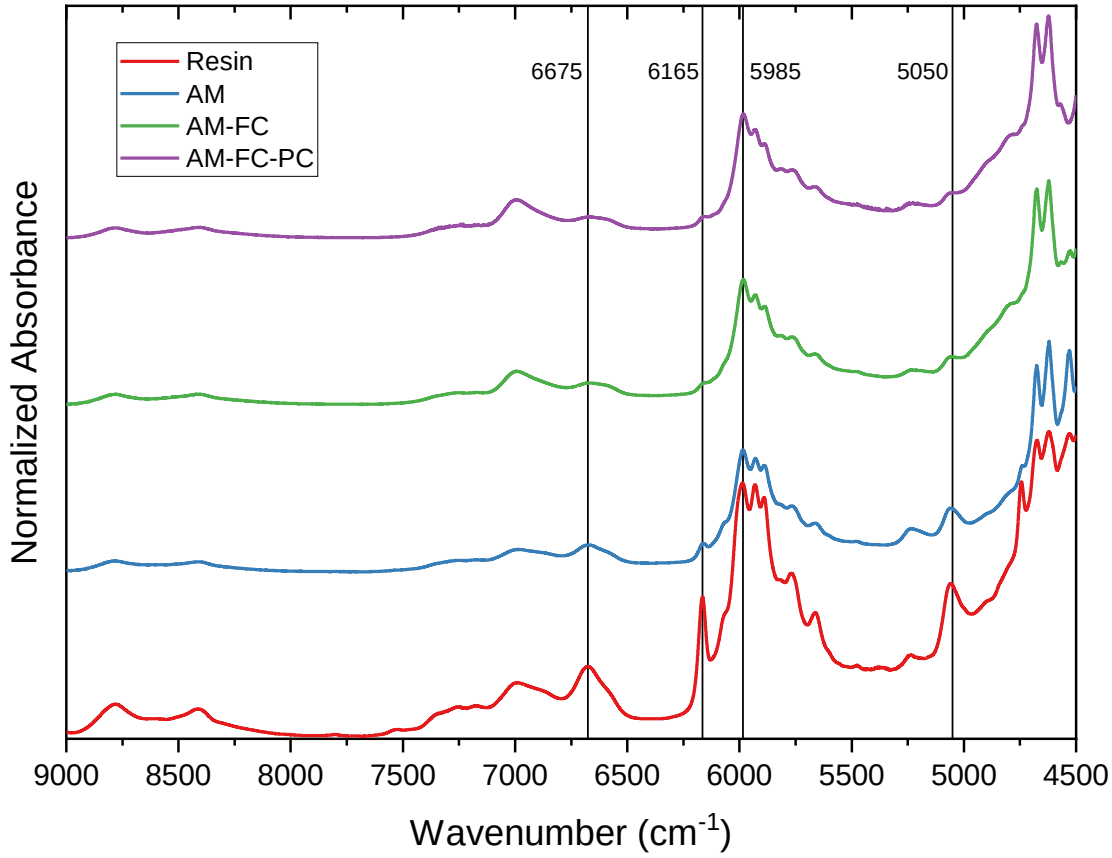

Figure A3

Exemplar FTIR Spectra for 300 µm Edge Matrix Samples

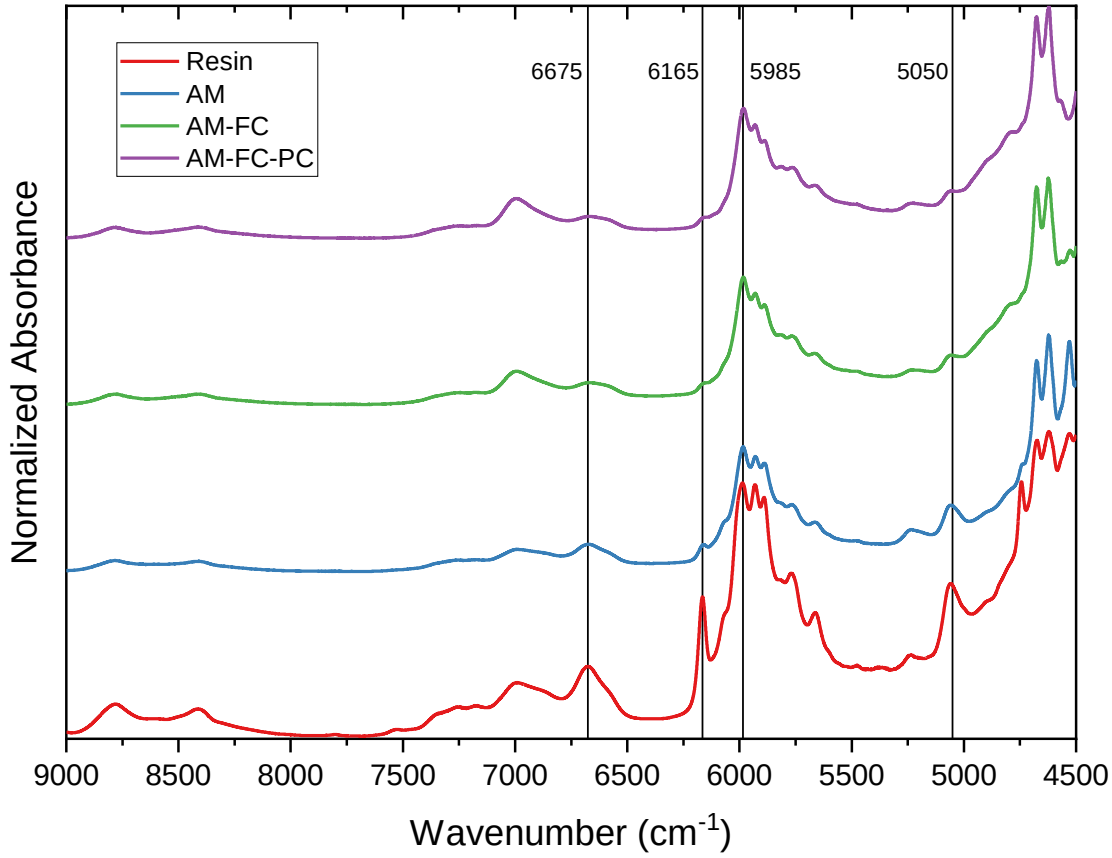

Figure A4

Exemplar FTIR Spectra for 200 µm Flat Matrix Samples

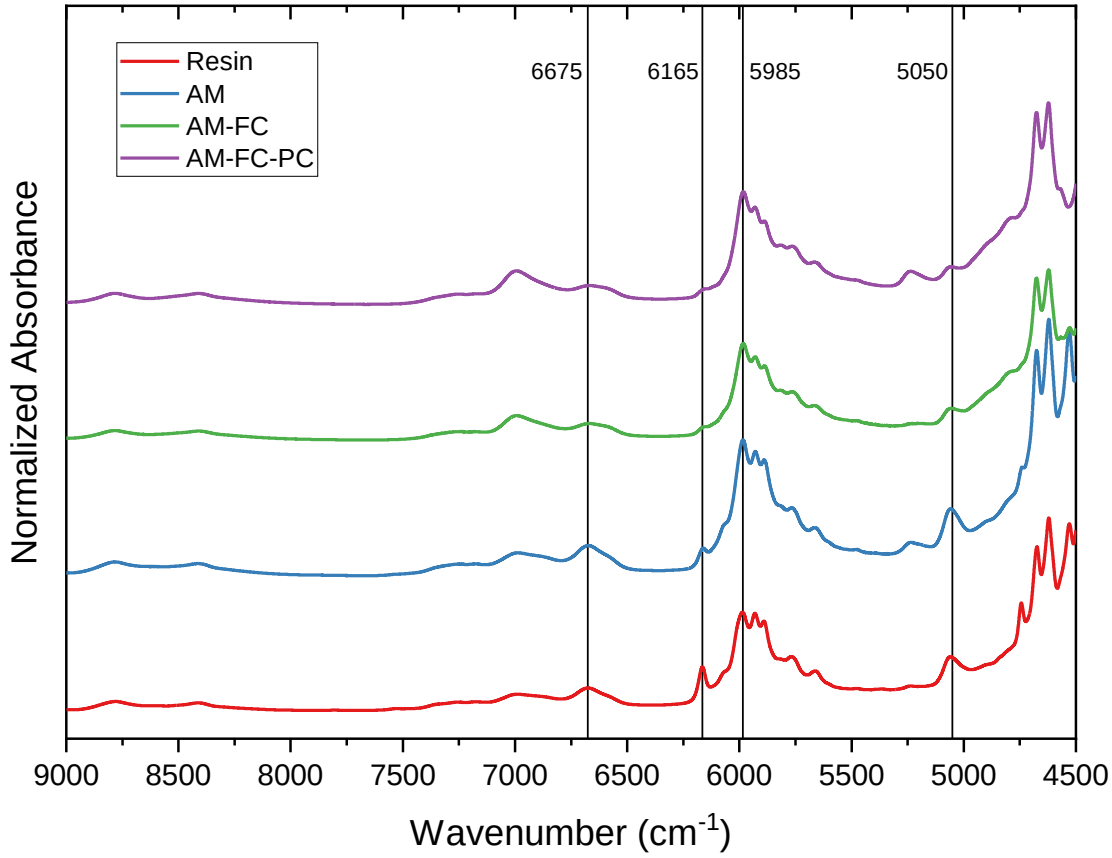

Figure A5

Exemplar FTIR Spectra for 25% FL, 200 µm, Edge, 70 s Samples

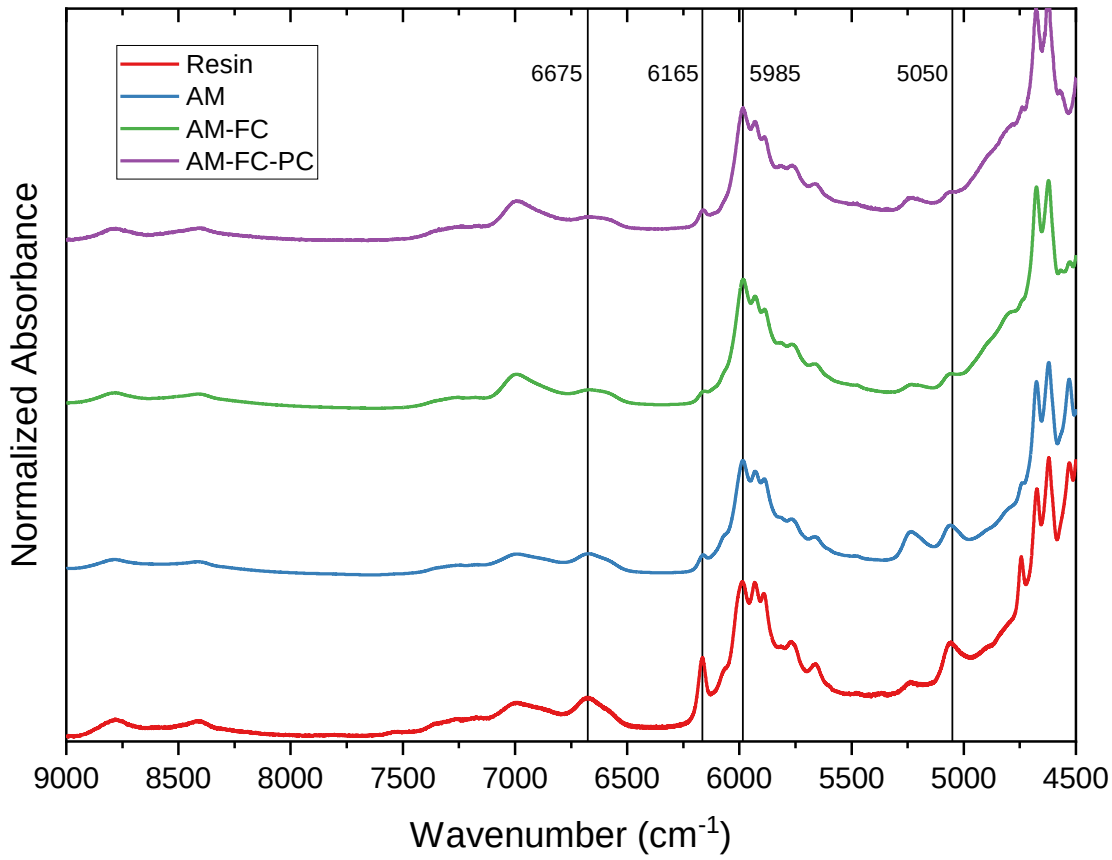

Figure A6

Exemplar FTIR Spectra for 25% FL, 200 µm, Edge, 90 s Samples

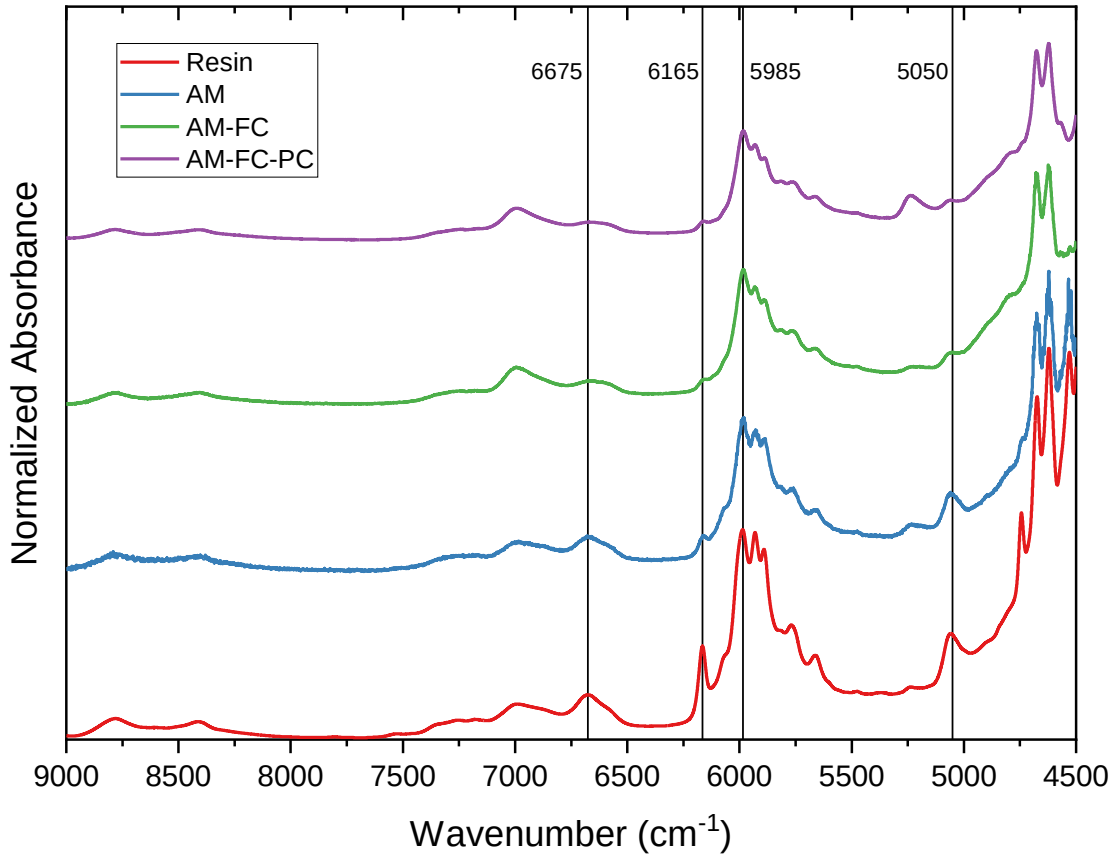

Figure A7

Exemplar FTIR Spectra for 25% FL, 200 µm, Flat, 70 s Samples

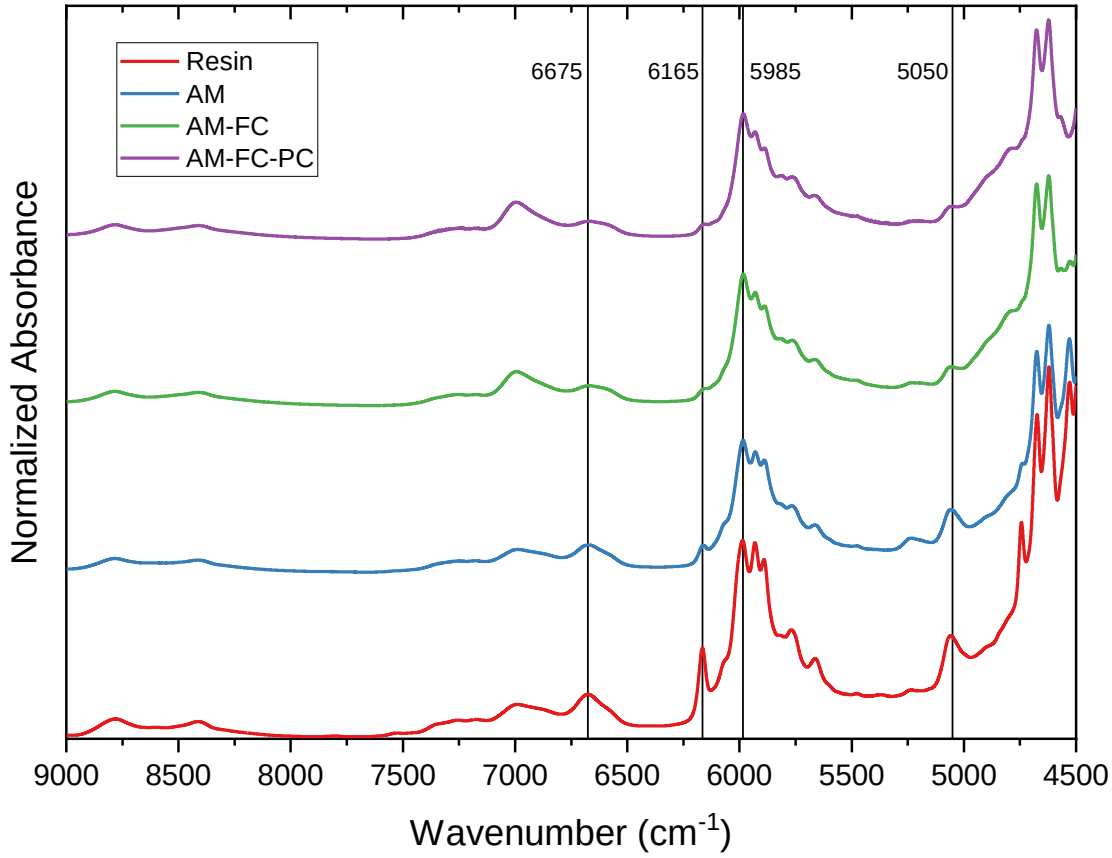

Appendix B

Printer Components

Table B1

Printer Prototype 2 Components

Component	Manufacturer
4040 Aluminum Extrusion, 25” x8	80/20 Inc.
4040 Aluminum Extrusion, 30” x4	80/20 Inc.
BenQ HT2550 Projector	BenQ
Megatronics V3.0 Microcontroller Board	RepRap
Raspberry Pi 3B+	Raspberry Pi
LTROP 24V 15A DC Power supply, 360W Switching Power Supply Transformer	LTROP
DRV8825 Stepper Motor Driver Carrier, High Current, x3	Polulu
2TK3GN-AW2U Torque Motor	Oriental Motor
2GN3SA Gearhead Parallel Shaft 3:1	Oriental Motor
PAVR-20KZ External Speed Potentiometer	Oriental Motor
TMP-1 Power Controller for Torque Motors	Oriental Motor
PKP244D15A2 1.65 in. 2-Phase Bipolar Stepper Motor	Oriental Motor
Torque-Limiting Coupling for 1/4" Diameter Round Shaft, 16 in.-lbs. @ 50 rpm	McMaster-Carr
3/4" Diameter Conveyor Roller, Steel, for 10-3/8" Between Frame Width x8	McMaster-Carr
Rotating/Tilting Ball-Grip Positioning Arm	McMaster-Carr
Corner Machine Bracket with 4 Mounting Slots, 316 Stainless Steel, 100 mm x 60 mm x 75 mm, x8	McMaster-Carr

Component	Manufacturer
Mirror Front Plane – 3x5 in	VWR
Moai FEP Film Vat	Peopoly
Moai Servo Motor (tilt motor)	Peopoly
Moai Z-Axis	Peopoly
Moai Resin Vat Platform	Peopoly
Moai Build Platform, Attachment Bracket	Peopoly
Build Platform Base and Standoffs	custom
Spool Holder Bracket	custom
Spool Holder Spool Insert x2	custom
Torque Motor Bearing Bracket	custom
Bearing Holder x19	custom
Velocity Motor Bearing Bracket	custom
Velocity Motor Bracket	custom